Tectonics

RESEARCH ARTICLE
10.1029/2018TC004982

Key Points:
- Bending-moment normal faults strongly depend on the lithology of underlying beds, and to a lesser extent on the fold geometry and kinematics
- Fault-zone width, fault spacing, and efficiency in fold accommodation depend on bed thickness, interlimb angle, and fold kinematics
- Abundant bending-moment normal faults indicate that 4 km of fault slip is likely translated from the western Kunlun piedmont to the Mazatagh

Supporting Information:
- Supporting Information S1
- Table S1
- Table S2
- Table S3
- Table S4

Correspondence to:
T. Li,
litao.410@163.com

Citation:
Li, T., Chen, J., Thompson Jobe, J. A., Burbank, D. W., Cheng, X., Xu, J., et al. (2018). Active bending-moment faulting: Geomorphic expression, controlling conditions, Accommodation of Fold Deformation. *Tectonics*, *37*, 2278–2306. https://doi.org/10.1029/2018TC004982

Received 17 JAN 2018
Accepted 23 MAY 2018
Accepted article online 29 MAY 2018
Published online 3 AUG 2018

Active Bending-Moment Faulting: Geomorphic Expression, Controlling Conditions, Accommodation of Fold Deformation

Tao Li[1], Jie Chen[2], Jessica A. Thompson Jobe[3], Douglas W. Burbank[4], Xiaogan Cheng[5], Jianhong Xu[2], Zhigang Li[1], Wenjun Zheng[1], and Peizhen Zhang[1]

[1]Guangdong Provincial Key Laboratory of Geodynamics and Geohazards, School of Earth Sciences and Engineering, Sun Yat-sen University, Guangzhou, China, [2]State Key Laboratory of Earthquake Dynamics, Institute of Geology, China Earthquake Administration, Beijing, China, [3]Institute of Tectonic Studies, Department of Geological Sciences, University of Texas at El Paso, El Paso, TX, USA, [4]Department of Earth Science, University of California, Santa Barbara, CA, USA, [5]School of Earth Sciences, Zhejiang University, Hangzhou, China

Abstract Bending-moment faults and flexural-slip faults (FSFs), as two basic fault styles due to bending-related tangential longitudinal strain, extensively and prominently crop out as surface scarps in the Pamir-western Kunlun and southern Tian Shan regions, northwestern China. Characteristic geomorphic expression, favorable formation conditions, and the role in folding accommodation of active FSFs have been systematically summarized in our recent studies. Here we investigate similar properties for well-developed bending-moment normal fault (BMnF) scarps at four sites. Our study concludes the following: (i) BMnF scarps are relatively sinuous compared to FSF scarps and probably trend obliquely to the fold hinge. A group of BMnF scarps can delineate a single asymmetric graben or create grabens alternating with horsts. (ii) BMnF scarps primarily overlie poorly-layered conglomerates. The fold's interlimb angle can range from ~160° to <40°, and the folding kinematics can vary from active-hinge migration to fixed-hinge rotation. (iii) The fault-zone width, fault spacing, and efficiency in folding accommodation significantly decrease with (a) thinner conglomerate beds, (b) a smaller interlimb angle, and (c) the transition of the hinge from migrated to fixed. (iv) Different bed lithologies and fold geometries beneath the surface account for the predominance of BMnF scarps on the western Kunlun piedmont and FSF scarps in the Pamir-Tian Shan convergent zone. (v) Presence of BMnF scarps on the western Kunlun piedmont indicates that ~4 km of fault slip is transferred northward along a detachment at the base of the Cenozoic and is ultimately absorbed by the Mazatagh Thrust in the Tarim Basin.

1. Introduction

In thrust-related fold configurations, bending of beds typically generates tangential longitudinal strain (Figure 1a), which involves layer-parallel stretching in convex fold regions and layer-parallel compression in concave regions, with a neutral, no-strain surface separating these two parts (e.g., Davis et al., 2012; Fossen, 2010; Ramsay, 1967; Tavani et al., 2015). If the bed is well layered, the strain can be accommodated by flexural slip due to layer-parallel slip along weak contacts between beds (Figure 1b1). The slip direction is toward the anticlinal hinge and away from the synclinal hinge, whereas the slip amount, as a function of the bed dip and slip-surface spacing, attains a maximum on the fold limb but dies out at the fold hinge. Conversely, if the bed is relatively poorly layered such that layer-parallel slip is inhibited, the strain accommodation tends to alternate by bending-moment normal faulting at the fold crest and reverse faulting near the synclinal hinge due to local extension and contraction, respectively (Figure 1b2). At either site, the fault slip decreases to zero toward the neutral surface.

In areas dominated by active folds, flexural-slip faults (FSFs) and bending-moment faults (BMFs) can slice through the land surface and produce a series of subparallel, closely-spaced geomorphic scarps (Figure 1c; e.g., Audin et al., 2003; T. Li et al., 2016, 2017; Philip & Meghraoui, 1983; Yeats et al., 1997). Although the sense, orientation, and displacement of these faults cannot be extrapolated to those of the underlying causative thrust, they can provide useful information on folding kinematics (e.g., Ismat, 2008; T. Li et al., 2017; Salvini & Storti, 2004) and the paleoearthquake history of the underlying thrust (e.g., Gutiérrez et al., 2014; Kelsey et al., 2008; Livio et al., 2018; McCalpin, 2009). FSFs and BMnFs, as two typical secondary fault styles accommodating folding deformation, have been commonly observed in rock outcrops (e.g., Bazalgette et al., 2010;

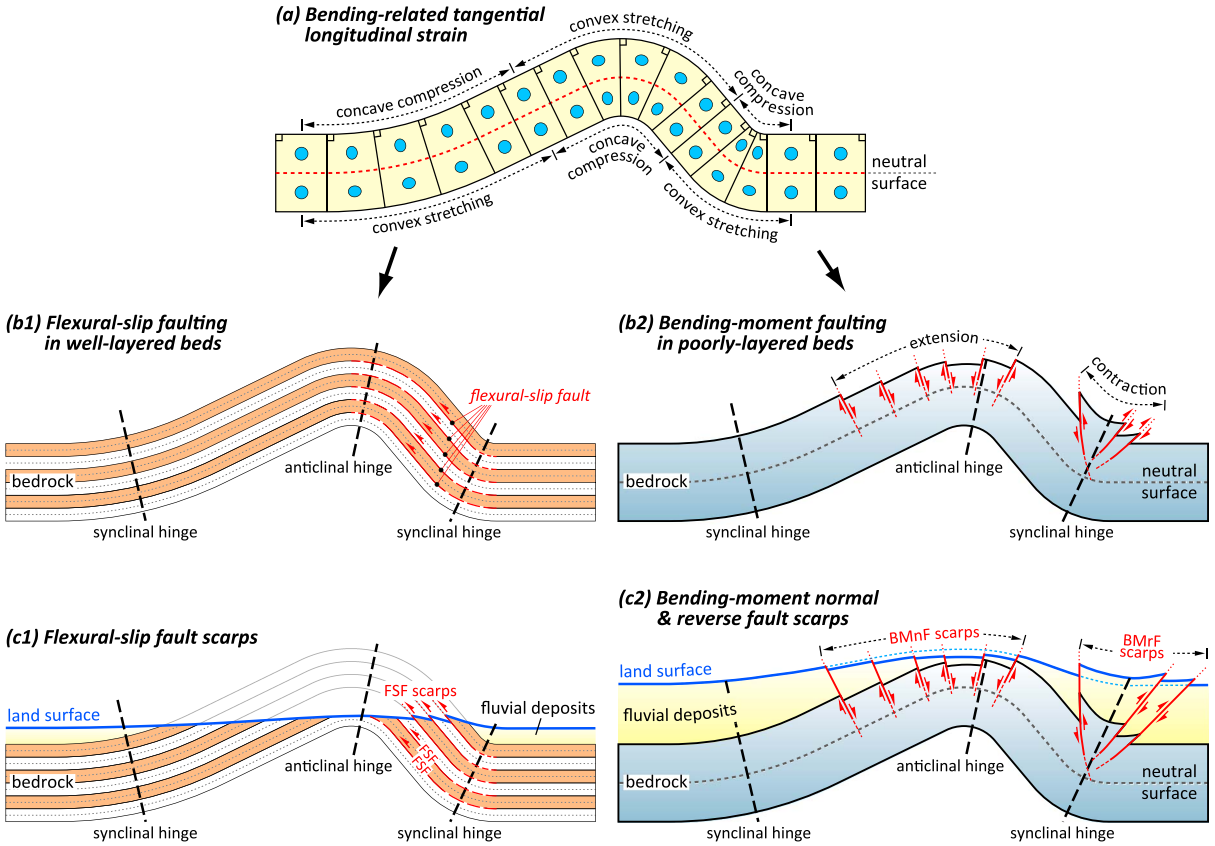

Figure 1. Flexural-slip and bending-moment faulting resulting from tangential longitudinal strain. (a) Distribution pattern of bending-related tangential longitudinal strain. The stretching convex-region is separated from the compressing concave-region by a neutral surface. The tangential longitudinal strain can either produce flexural slip in well-layered beds (b1) or produce bending-moment normal faults (BMnFs) at the convex part and reverse faults (BMrFs) at the concave part in poorly-layered beds (b2). Flexural slip and bending-moment fault slip decrease toward the hinge and neutral surface, respectively. Flexural slip (c1) and bending-moment faults (c2) cut through the land surface to produce geomorphic scarps. Referring to Fossen (2010) and to Yeats et al. (1997). FSF = flexural-slip fault.

Fischer & Jackson, 1999; Gutiérrez-Alonson & Gross, 1999; Horne & Culshaw, 2001; Tanner, 1989). Their associated geomorphic scarps, however, appear to be highly limited, especially the BMnF scarps: to date, very few and only brief case studies have been reported (Audin et al., 2003; McCalpin, 2009; Yeats et al., 1997). This data gap inhibits our investigations of, for example, geomorphic expressions, formation conditions, efficiency in accommodation of folding deformation, reliability in constraining the paleoearthquake history of the underlying causative thrust, and other basic questions associated with these faults.

The Pamir-western Kunlun and southern Tian Shan regions, northwestern China, are dominated by active thrusting and folding in their piedmonts and major intermontane basins (e.g., Allen et al., 1999; Goode et al., 2014; Huang et al., 2015; Hubert-Ferrari et al., 2007; T. Li et al., 2012, 2017; Saint-Carlier et al., 2016; Scharer et al., 2006; S. C. Thompson et al., 2002; Thompson-Jobe et al., 2017). Previous studies (Avouac & Peltzer, 1993; Heermance et al., 2008; Huang et al., 2015; T. Li et al., 2016, 2017) and our new surveys document numerous sets of well-developed FSF scarps and bending-moment normal fault (BMnF) scarps (Figure 2). The majority of FSF scarps are present in the western corner of the Tarim Basin where the Pamir and southern Tian Shan are converging at a high rate of ~7–11 mm/a (T. Li et al., 2012; Thompson-Jobe et al., 2017), whereas the majority of BMnF scarps are present on the western Kunlun piedmont, where the modern convergent rate is $<$2.0 mm/a. Through our recent work on prominent FSF scarps at eight sites (T. Li et al., 2015b, 2017), their geomorphic expression, diverse outcrop settings, and favorable conditions for formation (including bed lithology and dip, slip-surface spacing, and folding kinematics) have been investigated and systematically summarized. In this study we focus on the BMnF scarps at four sites: Slik, Cele, Haermodun, and Atushi. Based on observations of Google Earth images, geologic and geomorphic mapping, interpretations of seismic reflection profiles, integrated with differential GPS topographic measurements, we

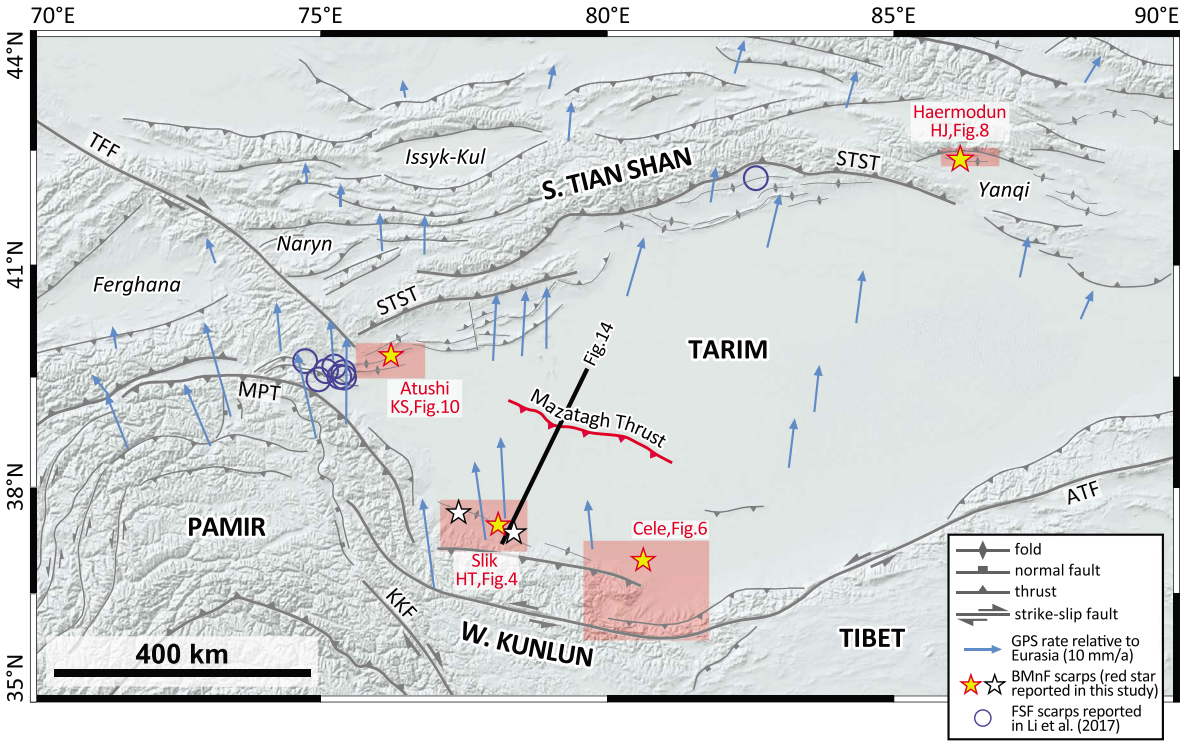

Figure 2. Topographic and structural map of the Pamir-western Kunlun and southern Tian Shan regions. Geodetic GPS arrows relative to stable Eurasia from Yang et al. (2008) and Zubovich et al. (2010). ATF = Altyn Tagh Fault; HJ = Hejing fold belt; HT = Hetian fold belt; KKF = Karakorum Fault; KS = Kashi fold belt; MPT = Main Pamir Thrsut; STST = Southern Tian Shan Thrust; TFF = Talas-Ferghana Fault.

surveyed BMnF scarps and associated geomorphic surfaces, as well as the underlying bed lithology, bed thickness, and fold geometry at above sites. Our work seeks to clarify the following questions:

1. What geomorphic expressions do these BMnF scarps have? What potential factors control their geomorphic expression?
2. Why do BMnF scarps predominantly crop out on the western Kunlun piedmont, whereas the FSF scarps are mainly concentrated at the western corner of the Tarim Basin? What bed lithologies, interlimb angles, and folding kinematics facilitate the presence of BMnF scarps? Do these factors differ significantly from those of FSF scarps?
3. To what extent can BMnFs accommodate fold deformation?

Based on field evidences that shape responses to these questions, we develop a conceptual model to compare and reconcile active bending-moment faulting and flexural-slip faulting in conjunction with folding deformation.

2. Active-Hinge Migration, Fixed-Hinge Rotation, and Bending-Moment Faulting

Folding-related kinematic models applied in this study include anticlinal active-hinge migration (Figure 3a1) and fixed-hinge rotation (Figure 3b). Theoretically, both kinematics can produce tangential longitudinal strain and BMnFs.

2.1. Active Hinge Migrated Fault Bend Fold

When a bed moves through a concave-downward fault bend, a kink band can develop between an anticlinal hinge and a synclinal hinge (Figure 3a1; Shaw et al., 2005; Suppe, 1983). The anticlinal hinge is pinned at the fault bend and is active with respect to the bed, representing a discontinuity in the uplift rate. Comparatively, the synclinal hinge is inactive and passively translated with the bed, across which the uplift rate remains constant. Consider a fluvial terrace lying above the fault bend (Figure 3a1): migration of the anticlinal hinge would differentially lift the fluvial terrace to produce a geomorphic fold scarp (Hubert-Ferrari et al., 2007; T. Li et al., 2015a; Scharer et al., 2006). With accumulation of fault slip and hinge migration, the fold scarp gradually increases its height and width, but its crest continues to be fixed with the anticlinal hinge. On either side of the fold scarp, different levels of fluvial terraces lie parallel with each other.

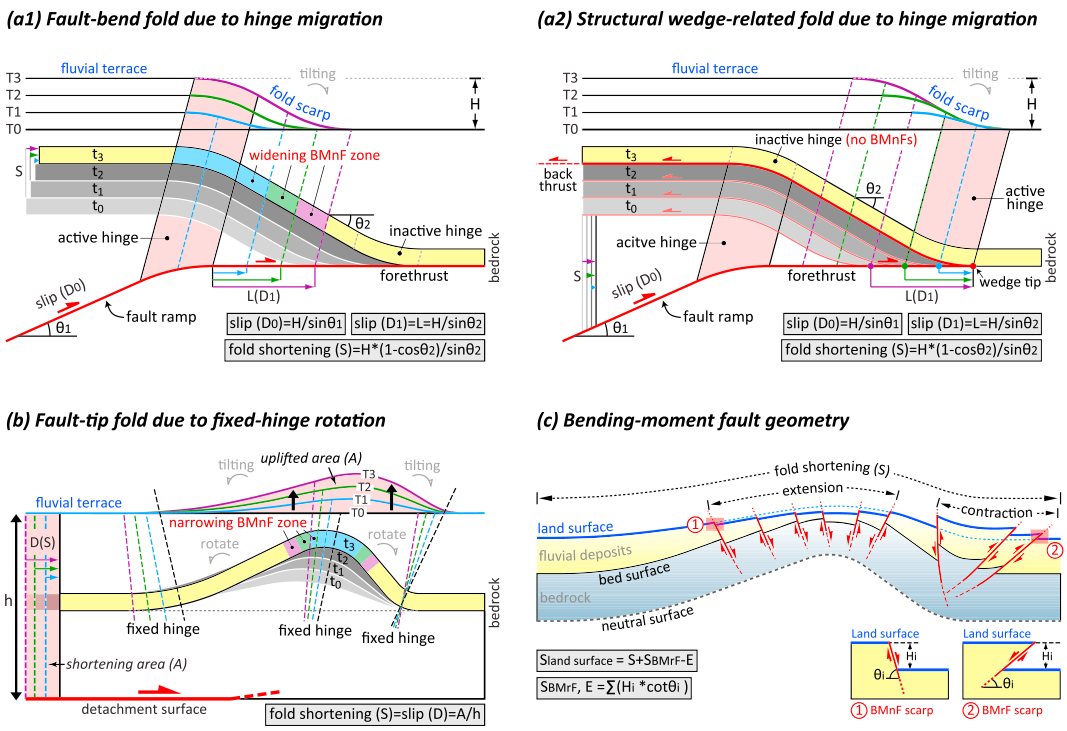

Figure 3. (a1, a2, and b) Terrace deformation pattern with different folding kinematics. Gray and yellow beds are before and after fold deformation, respectively. Terraces T3, T2, and T1 are respectively deformed during the bed moving from positions t_0 to t_3 (folded fluvial terrace, bending-moment normal fault (BMnF) zone and migrated or fixed hinge indicated by purple color), t_1 to t_3 (green), and t_2 to t_3 (blue), and terrace T0 indicates the modern riverbed. θ_1: fault ramp dip, θ_2: forelimb dip, *D*: fault slip, *L*: hinge migration distance, *S*: fold shortening. (a1) Fault-bend fold due to active-hinge migration. The bed that moves through an anticlinal hinge pinned at a concave-downward fault bend will develop a kink band at the forelimb and differentially lift the overlying fluvial terrace to produce a fold scarp. From T3 to T1 (old to young), fold-scarp height (*H*) increases gradually with progressive migration of the hinge relative to the bed. The fold-scarp crest is fixed with the anticlinal hinge, while the fold-scarp toe is passively transported with the underlying bed. Fluvial terraces are parallel with each other beyond the fold scarp. BMnFs can develop in the anticlinal hinge because of the bed moving and bending, but displacement will cease as soon as the bed moves out from the hinge. (a2) Structural wedge-related fold has a similar geometry to the fault-bend fold in Figure 3a1, except for a back thrust along the detachment on the hanging wall of the forethrust. The migrated synclinal hinge is pinned at the wedge tip and consequently fixes the fold scarp toes on different terrace levels. The anticlinal hinge above the back thrust is inactive such that no BMnFs can develop. (b) Fault-tip (fault-propagation and detachment) fold due to fixed-hinge rotation. The bed and the fixed hinge rotate to steepen the fold limbs, decrease the interlimb angle, and tilt overlying fluvial terraces. Progressive rotation causes successively emplaced terraces (T3 to T0) to fan in each limb. The structural relief (*A*) enveloped by a fluvial terrace is balanced with the shortening area (*A*) of a horizon at the same level of the fluvial terrace. BMnFs can be produced at the fold crest, but are likely confined in a narrower zone with continuing limb rotation. (c) Bending-moment fault geometry. Shortening (S_{BMrF}) or extension (*E*) accommodated by bending-moment faults is equal to the summed horizontal component of the dip slip along each fault. Net shortening ($S_{land\ surface}$) of the fold at the land surface is contributed by fold shortening (*S*), shortening (S_{BMrF}) accommodated by BMrFs, and extension (*E*) accommodated by BMnFs. θ_i = fault dip; H_i = fault-scarp height.

As a consequence of shortening during folding deformation, the slip along the fault ramp decreases across the fault bend. The fault slip prior to (D_0) and after (D_1: equal to the hinge migration distance *L*) passing through the fault bend can be calculated by the uplift of the bed or the overlying fold-scarp height (*H*) (Figure 3a1):

$$D_0 = \frac{H}{\sin\theta_1}, \tag{1}$$

$$D_1 = \frac{H}{\sin\theta_2}, \tag{2}$$

where θ_1 and θ_2 are the thrust ramp dip and forelimb dip, respectively. For the classical fault-bend fold, these two dips have a predicted geometric relationship (Suppe, 1983). The fold shortening, because of the bed migrating through the hinge to enter the kink band at the forelimb, can be calculated by (T. Li et al., 2015a):

$$S = H\times(1 - \cos\theta_2)/\sin\theta_2 \tag{3}$$

When the thrust ramp or forelimb is gentle (<20°), the fault slip consumed by folding deformation is minimal, and the major slip is transferred beyond the fold along the flat forethrust.

As illustrated in Figure 3a1, the moving and bending of the bed in the anticlinal hinge can amplify the bed curvature to generate BMnFs (Salvini & Storti, 2004; Tavani et al., 2015), even though the fold's interlimb angle remains constant. Progressive migration of the bed into the hinge zone generates new faults and increases the fault-zone width. Nonetheless, slip along these faults ceases immediately after the bed moves from the hinge into an adjacent dip panel. Geomorphic scarps generated by such faults on fluvial terraces can be formed within the fold scarp. An older terrace tends to have a wider fault zone, across which the fault-scarp heights remains relatively homogenous.

In structural interpretations, the fault-bend fold and structural wedge-related fold (in which a back thrust localized along the detachment connects with the forethrust and transfers the fault slip backward) are commonly difficult to distinguish due to their similar fold shapes (Figures 3a1 and 3a2). For the structural wedge-related fold, the active hinge is the synclinal hinge pinned at the wedge tip, whereas the anticlinal hinge above the back thrust is inactive (Shaw et al., 2005). Consequently, the fold-scarp toe is fixed with the synclinal hinge, and BMnFs are incapable of forming at the anticlinal hinge because none of the bed can move through the hinge to amplify the bed curvature. Therefore, patterns of terrace deformation and the presence or absence of BMnF scarps can allow us to discriminate between these two fold models. In this study, the BMnF scarps provide a critical reference in structural interpretations of the Slik and Cele folds.

2.2. Fixed Hinge Rotation

Distinct from geometries with increasing limb length but with invariant interlimb angle during active-hinge migration, the kinematics of fixed hinge rotation can rotate the bed around a fixed hinge to tighten the fold, during which the limb length remains unchanged (Figure 3b; Poblet & McClay, 1996; Shaw et al., 2005; Suppe et al., 1997). Overlying fluvial terraces are then tilted in the same direction as underlying beds. A succession of young to old terraces thus tends to have increasing tilt angles (Scharer et al., 2006).

For the fault-tip (detachment and fault-propagation) fold dominated by fixed-hinge rotation (Figure 3b), the shortening can be estimated from the mass-conservation method assuming that the uplifted area enveloped by the folded fluvial terrace is equal to the shortening area (A) of a horizon at the same level of the fluvial terrace (Epard & Groshong, 1993). The shortening (S) and fault displacement (D) can be calculated by

$$S = D = \frac{A}{h}, \tag{4}$$

where h is the height of the horizon above the detachment (Figure 3b).

To evaluate the magnitude of limb rotation and to calculate the structural relief area recorded by fluvial terraces, the initial slope of geomorphic surfaces prior to deformation should be known. At Slik, Haermodun, and Atushi, this slope is assumed to be represented by the fluvial gradient of the modern river that actively flows through the fold (Figure 3). At Cele where geomorphic surfaces are dominated by alluvial fans, the initial slope is approximated by the slope of the fan segment lying immediately beyond the folding deformation.

In fixed-hinge rotation, BMnFs and their associated geomorphic scarps can develop at the fold crest where bed-curvature amplification and convex-surface stretching are at a maximum (Figure 3b; Salvini & Storti, 2004; Tavani et al., 2015). With increasing limb rotation, the fault zone is expected to be confined into a narrower zone and the fault spacing accordingly decreases gradually (Salvini & Storti, 2004).

2.3. Geometric Model of Bending-Moment Faulting

Bending-moment faulting can produce extension characterized by normal faults at the fold crest while contraction characterized by reverse faults at the synclinal hinge (Figures 1 and 3c). The extension at the convex region is subjected to be compensated by the contraction at the adjacent concave region on the same surface. If not, the shortening at the neutral surface would be unequal to the net shortening at the bed surface (Figure 3c).

Based on formulas (3) and (4), the fold-related shortening (S) of the land surface can be calculated. Because bending-moment and other styles of secondary faults have been neglected in the development of these two formulas, we hypothesize this shortening represents the shortening at the neutral surface without fault disruption. The net shortening ($S_{\text{land surface}}$) at the land surface, which comprises the fold shortening (S) of the

land surface plus the shortening (S_{BMrF}) of BMrFs but minus the extension (E) of BMnFs, can approximate the net shortening ($S_{bed\ surface}$) of the bed surface immediately beneath it (Figure 3c):

$$S_{bed\ surface} \approx S_{land\ surface} = S + S_{BMrF} - E \quad (5)$$

The extension (E) and shortening (S_{BMrF}) can be easily estimated if the scarp height (H_i) and dip (θ_i) of each BMF are known

$$S_{BMrF}, E = \sum (H_i \times \cot\theta_i) \quad (6)$$

Therefore, the ratio between the extension (E) accommodated by BMnFs and the fold shortening (S) at the neutral surface can be used to evaluate the contribution of bending-moment faulting to the overall folding deformation.

3. Geologic Setting

In response to the Indo-Eurasian collision, deformation initiated in the Pamir-western Kunlun and southern Tian Shan regions during the late Oligocene-early Miocene (e.g., Cao et al., 2015; Dumitru et al., 2001; Sobel et al., 2006, 2013; Yin et al., 1998) and subsequently propagated toward the Tarim and major intermontane basins (e.g., Issyk-Kul, Naryn, and Yanqi Basins) to produce a series of foreland fold-and-thrust systems (e.g., the Hetian fold belt at the western Kunlun front, the Kashi fold belt at the southern Tian Shan front, and the Hejing fold belt in the Yanqi Basin) (Figure 2; e.g., Allen et al., 1999; Cheng et al., 2017; Heermance et al., 2008; J. A. Thompson et al., 2015; X. Wang et al., 2011). Presently, the piedmont regions of these mountains are dominated by active thrusting and folding, whose mechanisms include emergent thrusting (Grützner et al., 2017; Hubert-Ferrari et al., 2005; Y. Li et al., 2012; Thompson-Jobe et al., 2017), active-hinge migration (Goode et al., 2014; Hubert-Ferrari et al., 2007; T. Li et al., 2017; S. C. Thompson et al., 2002), fixed-hinge rotation (e.g., Huang et al., 2015; T. Li et al., 2013, 2017; Saint-Carlier et al., 2016; Scharer et al., 2006), flexural-slip faulting (T. Li et al., 2017), and bending-moment normal faulting.

As a result of vigorous exhumation and erosion of the surrounding mountains (Figure 2), the piedmont regions were infilled by a coarsening upward Cenozoic sedimentary sequence (Jia et al., 2004). The thickness of this sequence is up to 8–12 km thick in the western Kunlun piedmont and in the Pamir-Tian Shan convergent zone (Cheng et al., 2017; Jia et al., 2004; Scharer et al., 2004; Wei et al., 2013) but decreases significantly to $<$8 km in the southeastern Tarim Basin (H. Chen et al., 2009; Cheng et al., 2008) and $<$ 4 km in the Yanqi Basin (Li, 2002). The sedimentary fill is characterized by gypsum, limestone, or mudstone in the Paleogene, by interbedded sandstone, siltstone, and uncommon conglomerates during the Mio-Pliocene, and finally by massive, poorly-layered conglomerates of late Pliocene to Pleistocene age.

4. Methods of Data Collection

BMnF scarps were recognized and mapped in detail based on observations of Google Earth copyright images and additional field calibrations. At Slik (Figure 2), trench outcrops explicitly reveal that the upthrown side of geomorphic scarps occurs on a fault's footwall, indicative of normal fault displacement. Without field verification from well-exposed outcrops at the other three sites, we classified geomorphic scarps as BMnF scarps according to their typical features (e.g., Fossen, 2010; Livio et al., 2018; Tavani et al., 2015; Yeats et al., 1997): (i) they are commonly located at the fold crest; (ii) the scarps are numerous and closely spaced and are expressed by grabens alternating with horsts; and (iii) BMnF scarps strike approximately parallel with the axis of fold elongation. BMnF scarps are also easily distinguished from river-cut terrace risers because they are commonly perpendicular to the local drainage system.

For each field site, the overall fold geometry was defined by combining diverse data sets. At Slik and Cele (Figure 2), the fold expressions are unclear on the surface, and lithified beds are poorly exposed. There we collected and interpreted two high-quality 2-D seismic profiles across the folds to constrain their subsurface geometries. The depth conversion of the profiles assumes a uniform velocity of ~5,000 m/s, according to constraints from borehole measurements in Guilbaud et al. (2017). At Haermodun and Atushi where seismic

profiles are unavailable, geologic mapping of bed outcrops allows us to draw preliminary fold transects and define simplified near-surface fold geometries.

Notably, the bed lithology and thickness immediately beneath BMnF scarps play a critical role in controlling the style of bending-related faulting (Figure 1). We defined these characteristics through a combination of observations at bed outcrops, published logs of adjacent stratigraphic sections (Jia et al., 2004), interpretations of seismic profiles (Cheng et al., 2008; Li, 2002; Lu et al., 2016; B. Yang, 2004), and available borehole data (Jia et al., 2004; Lu et al., 2016).

Fluvial terraces and alluvial fans can serve as passive strain markers that record recent folding and faulting deformation. We divided such geomorphic surfaces into several main groups on the basis of (i) their elevation relative to each other and the modern riverbed and (ii) their surface morphology (older surfaces characterized by more developed desert pavement and higher degree of post-abandonment stream dissection). The topography of terrace treads and fault scarps was measured using a real-time kinematic differential GPS system with vertical resolution of $<$4 cm. This data set is capable of precisely recording deformation signatures across the entire fold. The deformation pattern of geomorphic surfaces, when correlated with the subsurface fold geometry, enables us to properly define both folding kinematics and magnitude of deformation.

Several trench outcrops at Slik reveal BMnF dips of 70–80°. In the absence of fault outcrops at other sites, this dip is used to represent the dip of all BMnFs at all study sites.

5. The Slik Monocline in the Hetian Fold Belt

The Hetian fold belt lies along the piedmont of the western Kunlun range (Figures 2 and 4a). On the surface, the fold belt rises through piedmont alluvium and produces a group of SE-SEE-trending warps with low topographic relief. Lithified bed exposures only include poorly layered Plio-Pleistocene conglomerate and scattered interbedded sandstone and mudstone of the Paleogene-Pliocene. Despite unclear surface expression, the gentle and broad fold geometries in the Cenozoic sequence, stacked thrust ramps in the Paleo-Mesozoic sequence, and two detachments localized at the bases of the Cenozoic and Paleozoic units are well imaged on petroleum seismic profiles (Figure 4b; e.g., Cheng et al., 2017; Guilbaud et al., 2017; Jiang et al., 2013; T. Li et al., 2016; Liang et al., 2012). Within the Hetian fold belt, BMnF scarps have been detected in the Guman, Slik, and Yaheshtagh folds (Figure 4a). Our work is focused on the Slik fold along the leading edge of the fold belt, where such scarps are particularly well developed and preserved.

5.1. The Slik Monocline

Barely visible on satellite images (Figure 4a), the Slik fold can be roughly outlined by uplifted and folded alluvial deposits and very limited exposures of the Plio-Pleistocene conglomerate along major transverse valleys. The fold is orientated southeast for ~40 km between the north-flowing Bashlangan and Kuoshtagh Rivers. Its subsurface geometry (Figure 4b), revealed by a high-resolution seismic profile along the Pixina valley, is characterized by a relatively steep (~21°N) northern limb and a gentle (~5°N) southern limb, displaying an overall north-vergent monocline. This geometry is associated with a ~19°S-dipping thrust ramp stepping up from the lower detachment at the base of the Paleozoic unit to the upper detachment at the base of the Cenozoic unit (Ainscoe et al., 2017; T. Li et al., 2016). The interpretation of the fault ramp dip of ~19° and the forelimb dip of ~21° reflects a fault-bend fold that is formed by the hanging-wall beds migrating through the curved fault bend bounded by the anticlinal hinges *C* and *D* (Figure 3a1; Suppe, 1983). According to the uplift of ~1.4 km of the Paleogene unit whose thickness remains relatively constant across the fold, slip along the fault ramp and upper detachment is estimated to be ~4.3 and 3.9 km, respectively (formulas (1)–(2), Figure 3a). Despite the ~4 km slip amount, most of the slip is transferred beyond the fold, such that the shortening absorbed by the fold itself is only ~260 m (formula (3) and Figure 3a), an order of magnitude lower than the overall slip amount.

In previous interpretations, the fault slip along the upper detachment either (i) is transferred basinward along a forethrust localized at the upper detachment (Cheng et al., 2017; Guilbaud et al., 2017; Liang et al., 2012; Lu et al., 2016), or (ii) is sent back to the hinterland along the upper detachment, forming a structural wedge (Jiang et al., 2013; T. Li et al., 2016; C. Wang et al., 2014). As described below, the presence of BMnF scarps at the fold crest tends to support the first scenario, such that approximately 4 km slip is transferred basinward (Figure 4b). At shallower depths in the profile, the Plio-Pleistocene strata (the unit boundary referring to borehole data and interpretation of the same seismic profile in Lu et al., 2016) thin southward from ~4,300 to

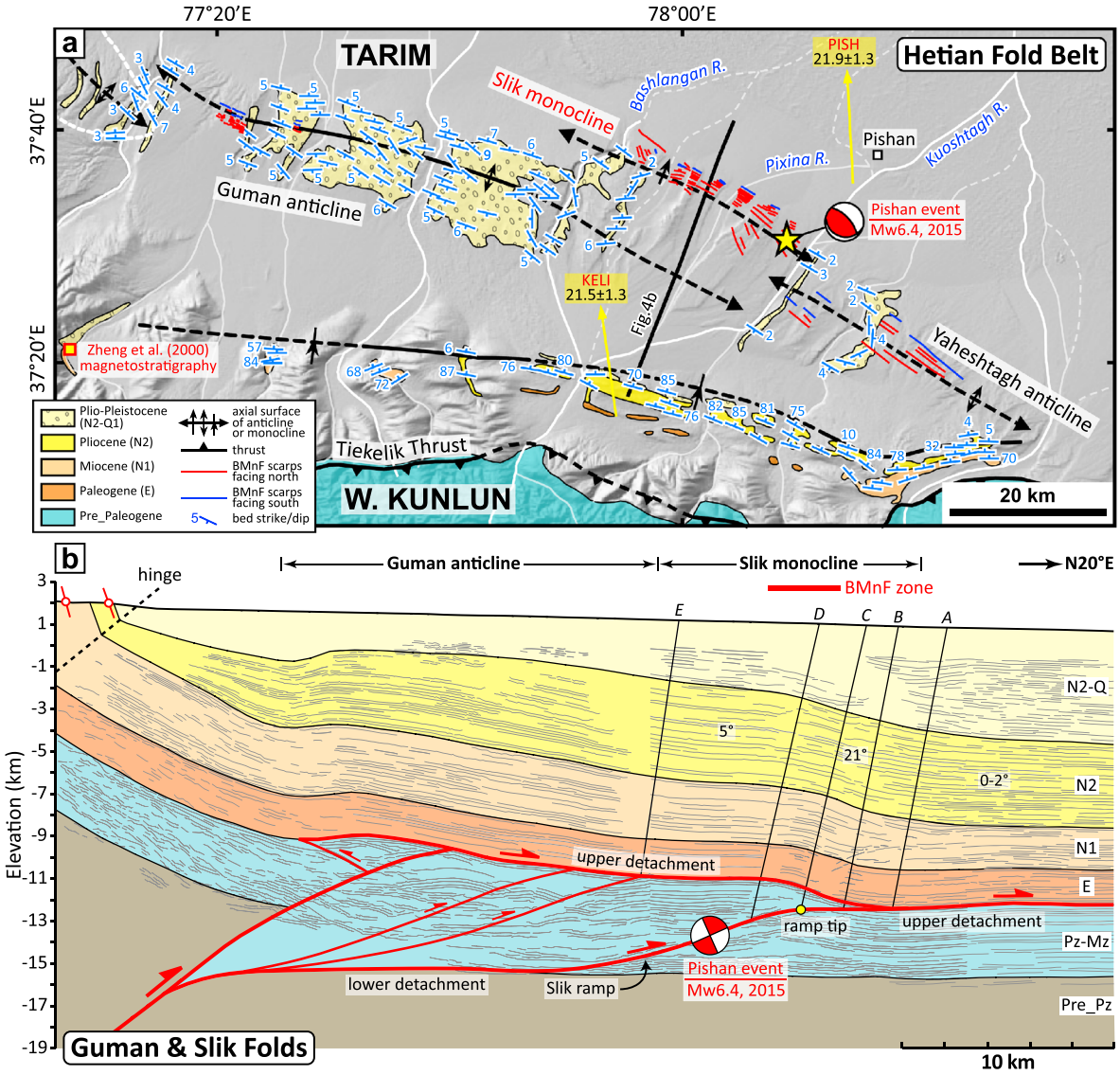

Figure 4. (a) Geologic map of the Hetian fold belt with locations of bending-moment normal fault scarps (see Figure 2 for the map location). Yellow arrows (named by PISH and KELI) show GPS velocities (mm/a) relative to the stable Eurasia (Zubovich et al., 2010). The epicenter and focal mechanism solution of the 2015 Pishan event from United States Geological Survey seismic catalog. Modified from T. Li et al. (2016). (b) Transects of the Slik and adjacent structures interpreted from a seismic reflection profile (indicated in Figure 4a). The unit boundaries refer to Lu et al. (2016). Lines *A*, *B*, *C*, *D*, and *E* are fold hinges separating dip panels. The uninterpreted seismic profile is available from supporting information in T. Li et al. (2016). The Slik ramp, controlling the overlying Slik monocline in the Cenozoic sequence, triggered the 2015 Pishan event (e.g., T. Li et al., 2016; Lu et al., 2016).

2,500–3,000 m to the fold crest, whereas the Pliocene strata keeps roughly constant in thickness (Figure 4b), documenting that the Plio-Pleistocene strata are growth strata and the Slik fold initiated at ~3.6 Ma based on stratigraphic correlation to a neighboring magnetostratigraphic study (the sampling section marked in Figure 4a; Zheng et al., 2000). The slip along the thrust ramp and the shortening of the Slik fold, therefore, have estimated average rates of ~1.2 mm/a and $<$ 0.1 mm/a, respectively.

The Slik fold was activated during the 2015 M_w 6.4 Pishan event. The seismicity (e.g., Ainscoe et al., 2017; T. Li et al., 2016) and geodetic observations (e.g., He, Wang, Ding, Wang, et al. 2016; He, Wang, Ding, Li, & Zou 2016) are compatible with the interpretation of a seismogenic Slik deep ramp (Figure 4b; T. Li et al., 2016; Lu et al., 2016). Coseismic and postseismic slips along the ramp are estimated to be 0.6–1.1 m and $\leq$ 0.4 m, respectively (Ainscoe et al., 2017; He, Wang, Ding, Wang, et al. 2016; He, Wang, Ding, Li, & Zou 2016). Nonetheless, such slip amounts produced no detectable surface fractures because the fault tip is buried as deep as ~14 km beneath the Cenozoic sediments.

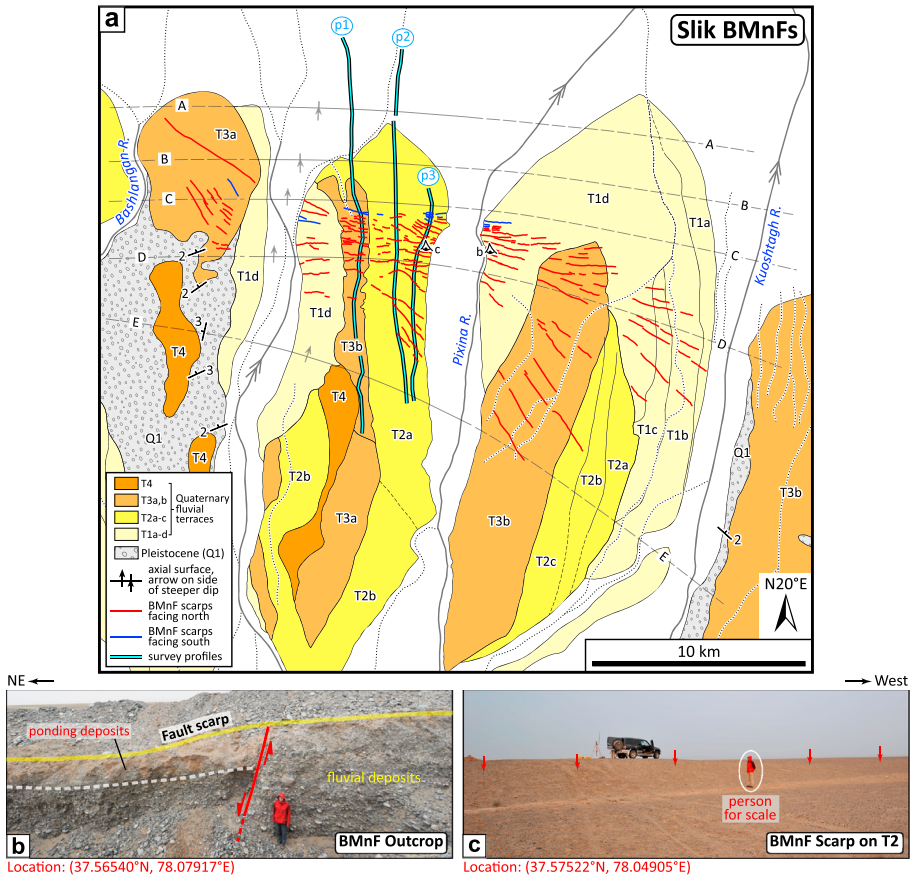

Figure 5. (a) Geologic and geomorphic map showing terrace treads, bending-moment normal fault (BMnF) scarps, and fold hinges *A*–*E* (determined from the seismic profile in Figure 4b) at the Slik fold. See Figure 4a for the map location. (b) A trench outcrop reveals that the geomorphic scarp is formed by a normal fault with a dip of 70–80°. Modified from T. Li et al. (2016). (c) Photograph of a BMnF scarp (marked by red arrows) on the T2 tread (viewpoint in Figure 5a). (d) Topographic survey profiles (locations in Figure 5a) of the T3b and T2a terrace treads and underlying fold geometry. The modern riverbed slope of −(0.7–0.8)° from Ainscoe et al. (2017). Lower panel: bed dips and fault dips with no vertical exaggeration (V:H = 1:1); upper panel: terrace tread slopes and BMnF dips vertically exaggerated.

5.2. Folding Deformation of Fluvial Terraces

Along the Bashlangan, Pixina, and Kuoshtagh valleys, ongoing folding has uplifted flights of fluvial terraces above the modern riverbed (Figure 5a). Each distinct terrace level has relatively high vertical separation within the fold, but the surfaces rapidly merge and are subsequently aggraded by recent deposits beyond the ramp-flat transition on the fold's north flank. It is challenging to confidently and specifically discriminate and correlate among these terraces because of their numerous levels and similar geomorphic characteristics. In geomorphic mapping, we amalgamated neighboring terraces with little vertical separation into one single level, subsequently divided these terrace amalgamations into four major groups. Based on cosmogenic ^{10}Be depth profile and luminescence dating (Guilbaud et al., 2017), the terraces T3b, T2a, and T1d were abandoned at >1,500, 220 ± 30, and 40 ± 3 ka, respectively.

The fluvial terraces have been significantly tilted (Figure 5d). Topographic survey profiles along the T3b and T2a treads to the west of the Pixina valley define slopes of −2.1 ± 0.1° and −1.4 ± 0.1° ("−" means northward sloping), respectively, overlying the forelimb of the fold. Relative to the modern fluvial gradient of −(0.7–0.8°) determined by Ainscoe et al. (2017), these two terraces are tilted ~1.4° and 0.7° to the north, respectively. In contrast, both terraces on the backlimb slope −0.7 ± 0.1°, close to the modern fluvial gradient, indicating no clear slope changes and tilting. This deformation pattern is generated as the fluvial terraces, in concert with the underlying beds, migrate through the curved fault bend, during which progressive terrace tilting occurs

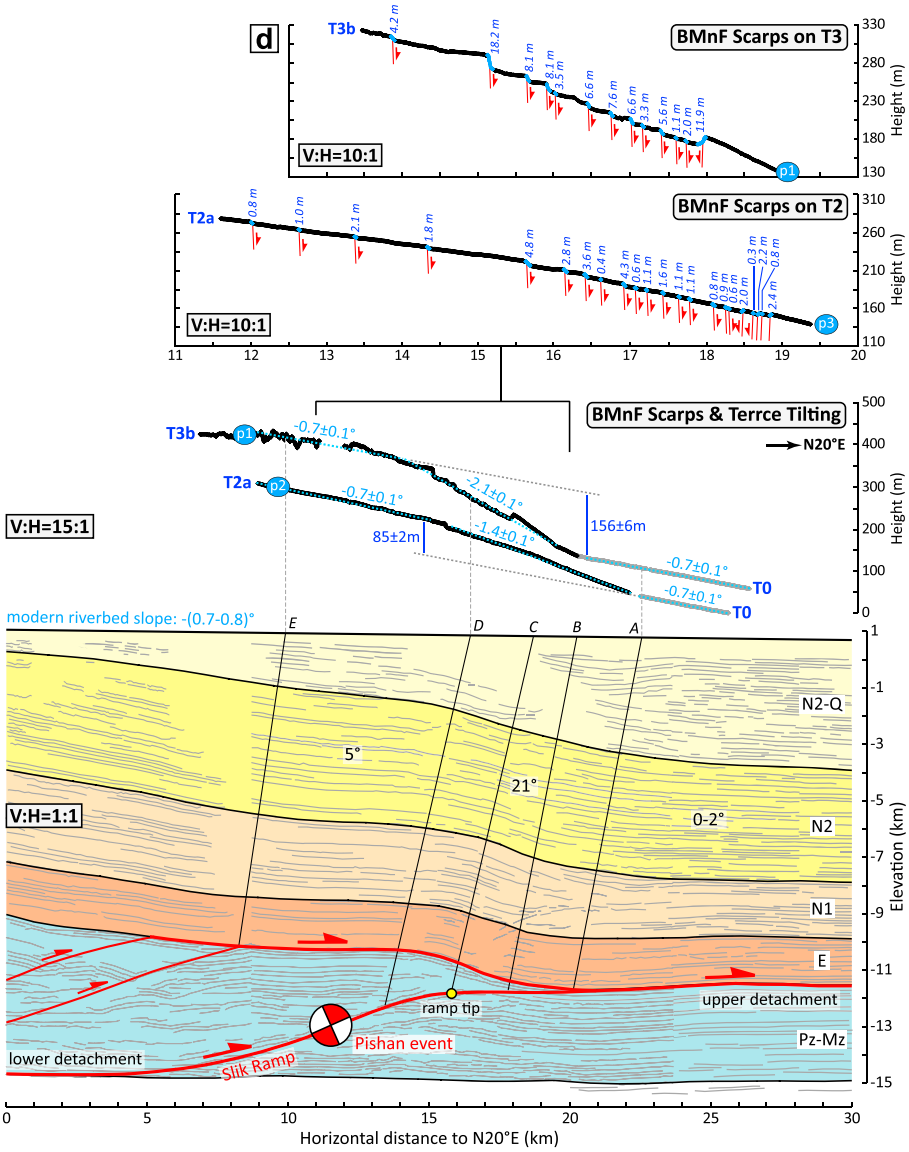

Figure 5. (continued)

(Figure 3a1). The structural relief of the T3b and T2a treads across the fold suggests vertical throw magnitudes of ~156 and 85 m on the deep thrust ramp, respectively. Because the northern parts of these two terraces are buried beneath recent deposits, these magnitudes represent minimum vertical throws on the thrust. According to formulas (1) to (3), the fault slip is estimated at ≥480 m and ≥260 m, and the shortening absorbed by the fold is ≥29 m and ≥16 m since the abandonment of the T3b and T2a treads, respectively. Using the terrace ages of >1,500 ka and 220 ± 30 ka constrained by Guilbaud et al. (2017), the slip rate along the fault ramp is 0.3–1.2 mm/a, roughly consistent with the average slip rate of ~1.2 mm/a since fold initiation. Given the estimated coseismic slip of 0.6–1.1 m during the 2015 Pishan event (Ainscoe et al., 2017; He, Wang, Ding, Wang, et al. 2016), the recurrence interval of earthquake with similar moment magnitude is estimated to be 500–3,600 years. The shortening rate accommodated by the Slik fold, however, is <0.1 mm/a.

5.3. Active Bending-Moment Faulting

On the tilted fluvial terraces, more than 20 subparallel BMnF scarps are present (Figure 5). The fault zone can be traced >25 km from the Bashlangan to Kuoshtagh water gaps. The overwhelming majority of the scarps face north, but a few face to the south, thereby defining an asymmetric or half graben. Correlation with the

underlying fold geometry indicates that such faults are located above the anticlinal hinge where the fold uplift is at a maximum (Figure 5d). Because BMnFs cannot be produced at the crest of a structural wedge-related fold, as illustrated in Figure 3a2, the existing BMnF scarps indicate that the Slik fold is a fault-bend fold.

From north to south, trends of fault scarps generally rotate from more E-W orientations toward more SE-NW orientations (Figure 5a): for example, the northernmost scarps trend N70°W in the west and gradually rotate eastward to N60°W, whereas the southernmost scarps rotate from trending N70°W to N20°W. Meanwhile, the fault zone widens from 4–6 km to up to 10 km, and the fault spacing increases from 40–1,300 to 200–1,700 m to the east. This rotation and spectacular fault-zone widening may arise because (i) the fold axis rotates clockwise, (ii) the cross-sectional fold geometry becomes gentler and wider and the folding rate decreases to the east, and/or (iii) a larger dextral shear component occurs on the eastern segment of the underlying Slik ramp as a result of interactions with the adjacent Yaheshtagh anticline (Figure 4a). Discrimination among these options, however, cannot be determined due to the lack of sufficient bedrock outcrops and subsurface data.

The scarp heights are 1.1–18.2 m (6.8 ± 4.3 m in average) on the T3b tread and 0.3–4.8 m (1.7 ± 1.2 m in average) on the T2a tread, displaying relatively constant height across the entire fault zone (Figure 5d). The summed heights of 13 fault scarps along the profile *p*1 and of 21 fault scarps along the profile *p*3 are ~87 m and ~35 m, respectively. Based on the fault dip of 70–80° revealed by trench outcrops (Figure 5b), the extension is estimated to be 15–32 m and 6–13 m (formula (6)), respectively. These values are comparable to the estimated fold shortening of ≥29 m (T3b) and ≥ 16 m (T2a), respectively, implying negligible shortening on the land surface overall (formula (5) and Figure 3c).

These BMnFs produced no clear surface rupture during the 2015 Pishan event. One possibility is that the coseismic slip was too small to be detected on the surface. Alternatively, such scarps cannot be produced by earthquakes with moment magnitude similar to the Pishan event (M_w 6.4), but instead by much larger earthquakes, which are probably generated by a simultaneous rupture beneath multiple folds, for example, the Guman, Yaheshtagh, and Slik folds sharing a common detachment (T. Li et al., 2016). Because the coseismic slip is either not apparent or even not present, the BMnF scarp is deemed incapable of preserving enough very recent coseismic or postseismic deposits at its front to record the Pishan event. This observation challenges the use of BMnFs to reconstruct the paleoearthquake history of active folds and associated blind thrusts (e.g., Livio et al., 2018; McCalpin, 2009).

6. The Blind Cele Fold

Approximately 200 km east of the Slik fold, a set of SE-trending normal fault scarps, named the Cele Fault, are conspicuous on the piedmont alluvium at the eastern extremity of the western Kunlun range (Figure 6a). On the basis of geomorphic mapping and tectonic regime analysis, Avouac and Peltzer (1993) proposed this fault represented a regional normal fault related to flexural subsidence of the Tarim Basin due to loading by the western Kunlun overthrust. Our collected seismic profile across this fault, however, definitely shows that the subsurface structure, instead of being a significant normal fault, is dominated by a gentle asymmetric fold (named Cele fold, Figure 6b), providing essential evidence for the genesis of these scarps by bending-moment faulting.

6.1. The Cele Monocline

The Cele fold is entirely buried beneath piedmont alluvium (Figure 6a). Even the north-flowing rivers, including Kulanmuleke, Outulake, Paheteleke, and Cele Rivers, flow across this blind fold without clear diversion (Figures 6a and 7a). The fold at depth is clearly revealed by continuous seismic horizons within the Cenozoic sequence (Figure 6b): a north-vergent monocline comprising a ~22°N-dipping northern limb and a subhorizontal southern limb. Underlying the fold, a ~19°S-dipping thrust ramp is identified by the direct fault-surface reflection and the presence of footwall cutoffs. This fault involves the pre-Paleozoic basement and climbs upward to a horizontal detachment localized at the base of the Cenozoic sequence. The fault bend is curved and can be correlated with the ~8°N dip panel bounded by hinges *B* and *C* (Figure 6b). Similar to the Slik fold, the Cele fold geometry is compatible with a fault-bend fold geometry (Suppe, 1983), and the BMnF scarps at the crest (described below) can serve to interpret that the slip along the deep ramp is transferred to the foreland rather than to the hinterland. South of the Cele fold, a blind monocline, with a geometry similar to the Cele fold, is also well illustrated on the seismic image (Figure 6b).

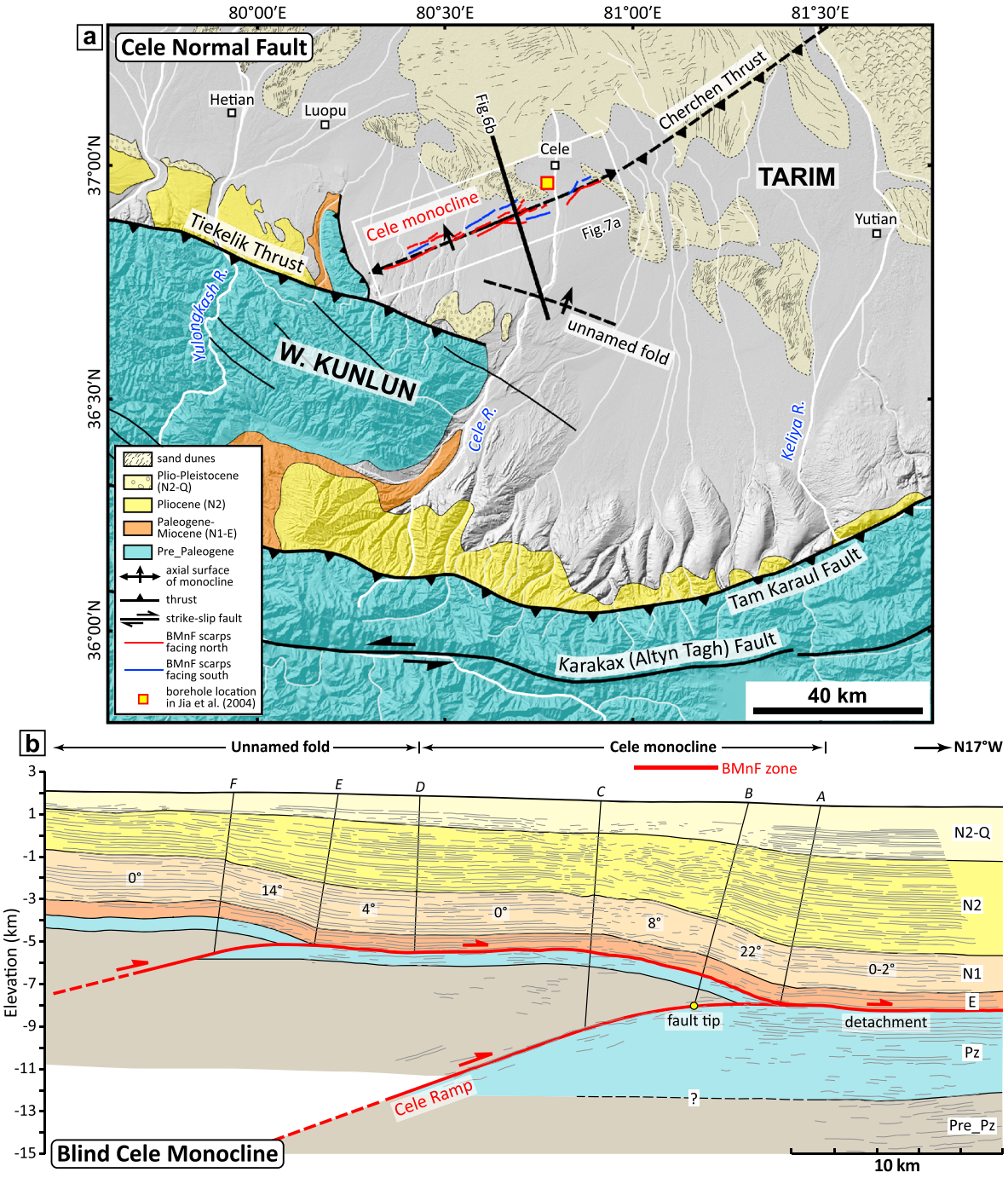

Figure 6. (a) Geologic map of the Cele Normal Fault and structures at its background (see Figure 2 for the map location). The strike of the blind Cele fold is speculated to parallel the fault scarps and the unnamed fold is speculated to extend along the area outlined by intense surface dissection. (b) Transects of the Cele and adjacent structures interpreted from a seismic reflection profile (shown in Figure 6a). The unit boundaries refer to descriptions of borehole data in Jia et al. (2004) and seismic interpretations in Cheng et al. (2008). Lines *A*, *B*, *C*, *D*, *E*, and *F* are fold hinges. BMnF = bending-moment normal fault.

According to the Cele fault ramp dip of ~19° (Figure 6b), the forelimb dip of ~22°, and the uplift of ~2.5 km of the Paleogene or Miocene unit, slip along the fault ramp and slip along the horizontal detachment are ~7.7 and 6.7 km, respectively, and the total shortening is ~500 m absorbed by the fold (formulas (1)–(3) and Figure 3a). The Cele fold initiated approximately at the beginning of the Pliocene (~5.5 Ma), as manifested by the tapering toward the fold crest (growth strata) of the Pliocene strata. Based on the Pliocene age, the average fault-slip rate and shortening rate are ~1.4 and $<$ 0.1 mm/a, respectively. Above the Pliocene unit, the

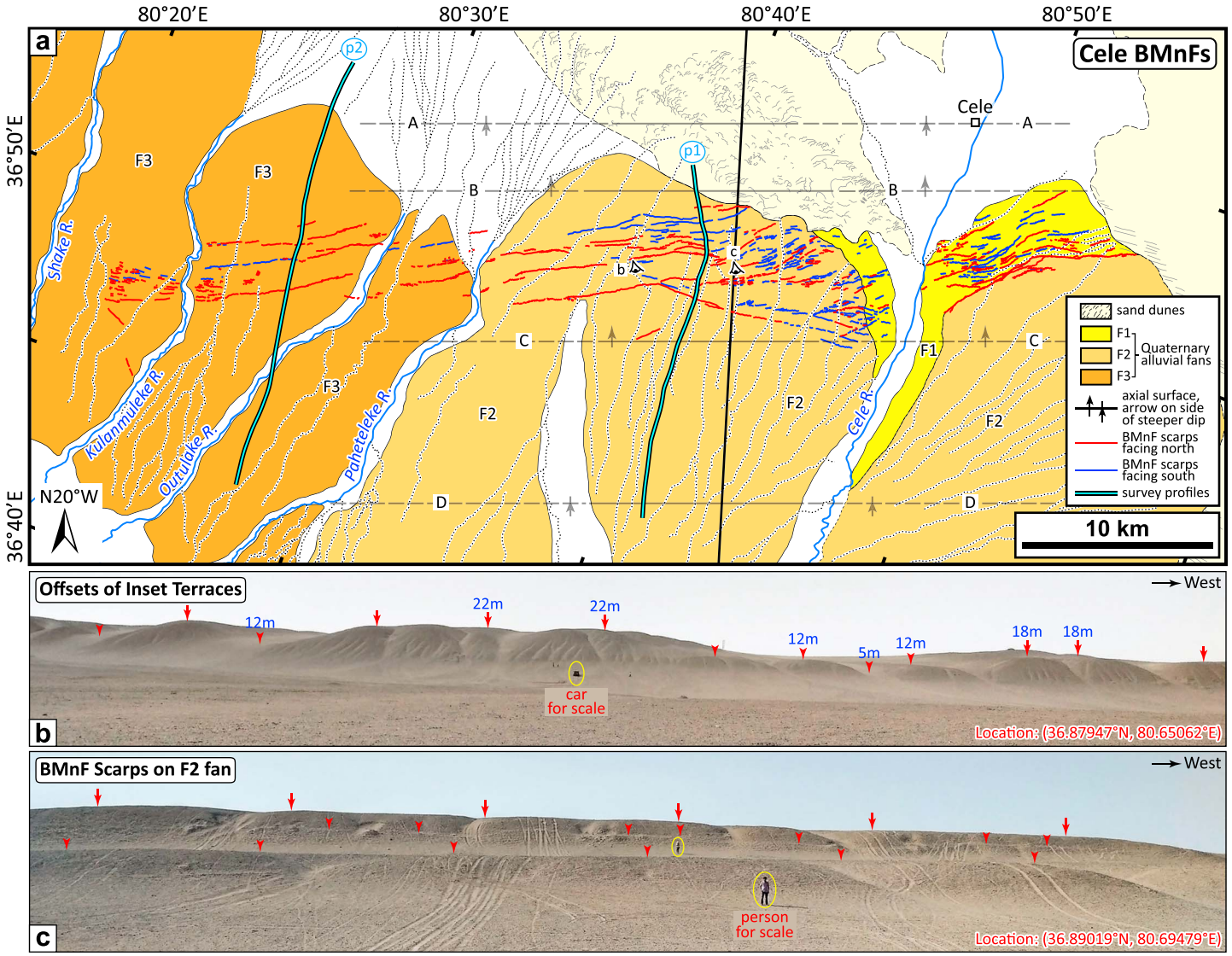

Figure 7. (a) Geomorphic map displaying alluvial fans, bending-moment normal fault (BMnF) scarps, and fold hinges *A*–*D* (determined from the seismic profile in Figure 6b) above the blind Cele fold. The stage classification of alluvial fans refers to Avouac and Peltzer (1993). (b) Photograph (viewpoint in Figure 7a) showing displacements of local inset terraces. The higher (older) terrace level records higher fault scarp. (c) Photograph (viewpoint in Figure 7a) of BMnF scarps on the fan F2 displaying a stair-step morphology. Red arrows mark the top of the BMnF scarps. (d) Topographic survey profiles (locations in Figure 7a) of the fans F3 and F2 and underlying fold geometry.

Plio-Pleistocene conglomerate is ~1,600-m thick at the fold crest (referring to descriptions of borehole data, see Figure 6 for the approximate location, in Jia et al., 2004, and seismic interpretations in Cheng et al., 2008).

The blind Cele and southern unnamed folds are probably the western continuation of the Cherchen thrust system, which is totally obscured by sand dunes in the Tarim Basin (Figure 6a). The thrust system includes several NE-trending, basement-involved thrusts with certain sinistral slip component and represents the forelandward propagation of the Altyn Tagh fault system (Figures 2 and 6a; Cheng et al., 2008; S. Yang et al., 2009).

6.2. Folding Deformation of Alluvial Fans

The piedmont alluvium can be approximately divided into three stages (Figure 7a). The uppermost fan F3 and Cele Fan F2 (named by Avouac & Peltzer, 1993) extend laterally for >30 km, compared to the lowest fan F1

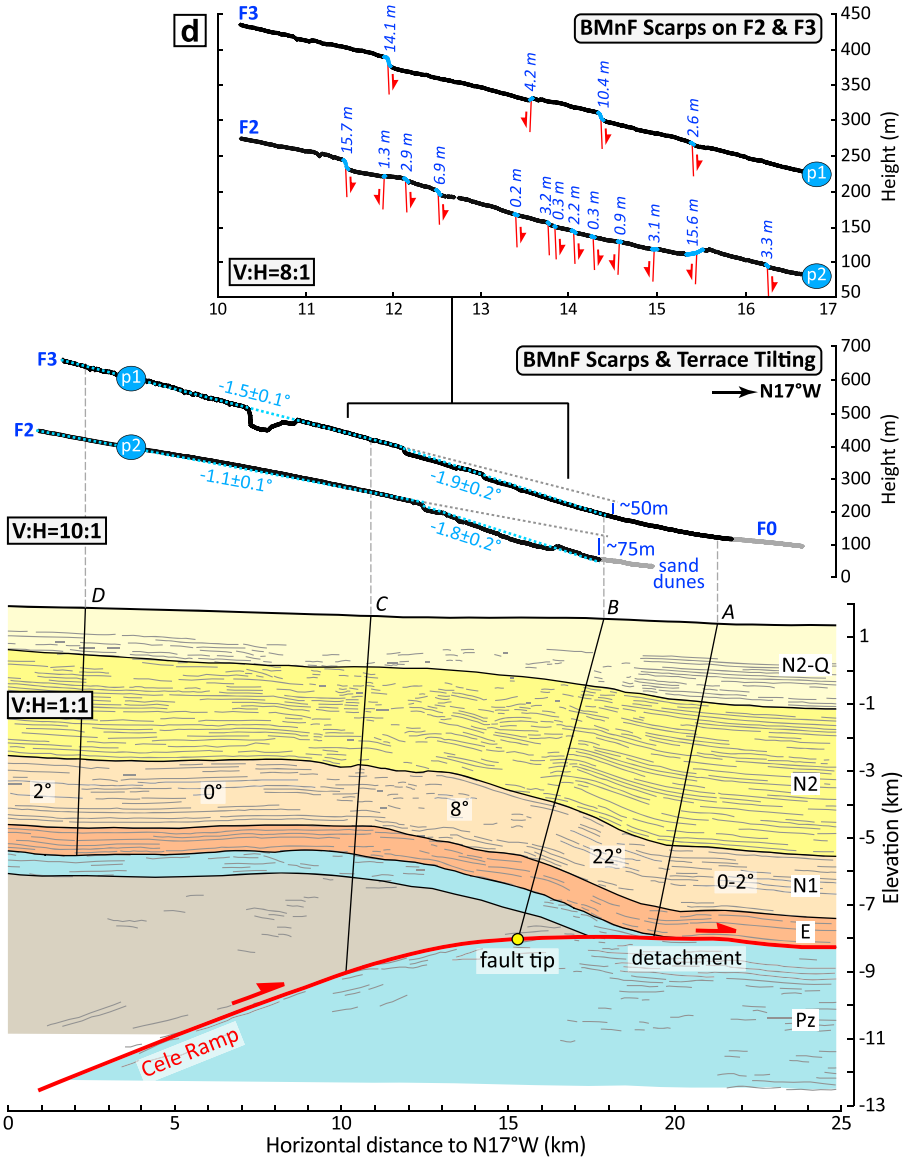

Figure 7. (continued)

that is limited to the immediate sides of the Cele River valley. These alluvial fans are generally planar and well preserved, although the north-flowing rivers dissect them to create steep, narrow gorges and successive nested fluvial terraces. Based on a regional correlation with dated alluvium in the upper Keliya River valley (Figure 6a, ~100 km southeast of Cele town) and an assumption of the alluvial fan emplacement during major glacier retreats, Avouac and Peltzer (1993) suggested a depositional age of 12–22 ka for the Cele Fan (F2).

We acquired topographic profiles on the fans F3 and F2 across the entire fold transect to underpin explicit analyses of the folding and faulting deformation (Figure 7d). On the fold's backlimb, beds maintain their original sedimentary dip of ~0°, indicating that the hanging wall is raised uniformly by the deep thrust ramp without clear rotation. Accordingly, the overlying alluvial fans are expected to be not tilted and to maintain their initial slopes. Compared to the slopes of $-1.5 \pm 0.1°$ and $-1.1 \pm 0.1°$ on the backlimb, the fans F3 and F2 are respectively tilted ~0.4° and 0.7° to the north on the forelimb, thereby lowering the height of alluvial surface by ~50 and 75 m, respectively. These heights represent a minimum structural relief above the thrust, because recent deposits bury the northern part of the measured fan (Figures 7a and 7d). It is noteworthy that both the tilt angle and structural relief recorded by the F3 fan are lower than those recorded by the F2 fan.

Being older than F2, the F3 fan must have experienced a longer period of folding deformation. On the basis of these data, we propose that the lower structural relief of the F3 than F2 fans reflects that fault slip and/or fault dip significantly decrease from the location of the profile *p*1 to *p*2.

Analogous to the Slik fold, the surface tilting on the forelimb can be attributed to fault-bend folding above the curved fault bend (Figure 3a1). The slip along the fault ramp is estimated to be ~230 m, and the shortening absorbed by the fold is only ~15 m since the abandonment of the F2 fan (formulas (1) and (3)). If we use the same fault-ramp dip of ~13° at profile *p*2, the fault slip and fold shortening are ~150 m and 10 m, respectively, recorded by the F3 fan. Combining with the age of 12–22 ka for the fan F2 proposed by Avouac and Peltzer (1993), the slip rate along the deep fault ramp is estimated to be ≥10 mm/a. This rapid rate seems unlikely, given that the low long-term shortening rate of 1–3 mm/a in the region (e.g., Cheng et al., 2017; Guilbaud et al., 2017; Jiang & Li, 2014), the modest or absence of surface expressions of active structures, the low convergent rate from geodetic GPS data (e.g., Gan et al., 2007), and the sparse modern earthquakes (e.g., T. Li et al., 2016) all suggest a low tectonic activity of the region. Therefore, the age of Cele Fan F2 may be significantly underestimated, and additional chronological work is required in order to place more confident constraints on the age of alluvial fans and deformation rates.

6.3. Active Bending-Moment Faulting

On satellite images, the Cele normal fault zone is expressed as a series of prominent, NE-NEE-trending linear scarps (Figures 6a and 7a), which can be easily distinguished from fluvial scarps, because they are commonly oriented perpendicular to each other. The fault zone overall extends northeast from the western Kunlun range front, cuts through major river valleys, and ultimately disappears beneath sand dunes near Cele town, with a total length of exceeding 50 km and a total fault-zone width of 3–7 km. Fault scarps are north facing or south facing, creating a landform characterized by horsts alternating with grabens.

Along its southwestern portion, the fault zone is dominated by three to five prominent, spaced 800–2,000 m apart, fault scarps (Figure 7a). The north-facing scarps are more prominent and higher than the south-facing ones. Along measured profile *p*2, scarp heights range from ~2.6 to 14.1 m (average 7.8 ± 4.6 m), with a summed height of ~31 m (Figure 7d). To the east, the fault scarps rapidly split into numerous branches (>20) that are more closely spaced (several tens of meters to 1 km), obliquely aligned, and occupy a much wider zone (~7 km). The south-facing scarps gradually increase in abundance and even outnumber the north-facing scarps along the western bank of the Cele River, whereas the overall relief of these scarps continues to lower to the north. The fault zone, as illustrated by profile *p*1, is characterized by a series of relatively low horsts and grabens (0.3–7.0-m high) defined by two major antithetic scarps with heights >15 m. A summed vertical offset of ~56 m is estimated to be recorded by the fan F2. On the seismic profile, BMnFs are indistinguishable because of their very small offsets (Figure 7d). However, the seismic horizons beneath these geomorphic scarps do not appear continuous as those farther away from it, probably attributable to the disruption of BMnFs. These fault scarps occur at the crest of the blind fold, validating our previous interpretation that the anticlinal hinge pinned at the fault bend is migrated and remains as the locus of bending deformation, and that the Cele fold is a fault-bend fold (Figure 3a1).

Fault scarps are dissected at a number of locations by ephemeral channels to create locally inset terrace levels on their upthrown sides. Such sites show clear records of increasing fault-scarp heights with terrace age. In the case shown in Figure 7b, the uppermost terrace (fan F2) and immediately lower terrace are vertically offset 21–22 and ~18 m, respectively, whereas the latest abandoned terrace level or channels that are partially covered by loess are vertically offset by ~12 or 5 m. This landform-offset pattern provides key evidence of multiple rupture events sourced by the Cele fold and the underlying thrust ramp. If the coseismic vertical offset is 1–2 m as documented by Avouac and Peltzer (1993), the uppermost terrace (fan F2) has likely experienced more than ten similar earthquakes since its initial abandonment.

In general, the fault scarps display a right-stepping *en echelon* pattern along the strike of the fault system. This pattern suggests some left-lateral shear of the Cele thrust ramp, consistent with the sinistral-slip component of the Cherchen thrust system that was interpreted in previous studies (e.g., Cheng et al., 2008; S. Yang et al., 2009). If we assign a fault dip of 70–80° (similar to that of the Slik BMnFs), the total extension defined by profiles *p*2 and *p*1 are 10–19 and 5–11 m, respectively, compatible with the shortening accommodated by the folding deformation.

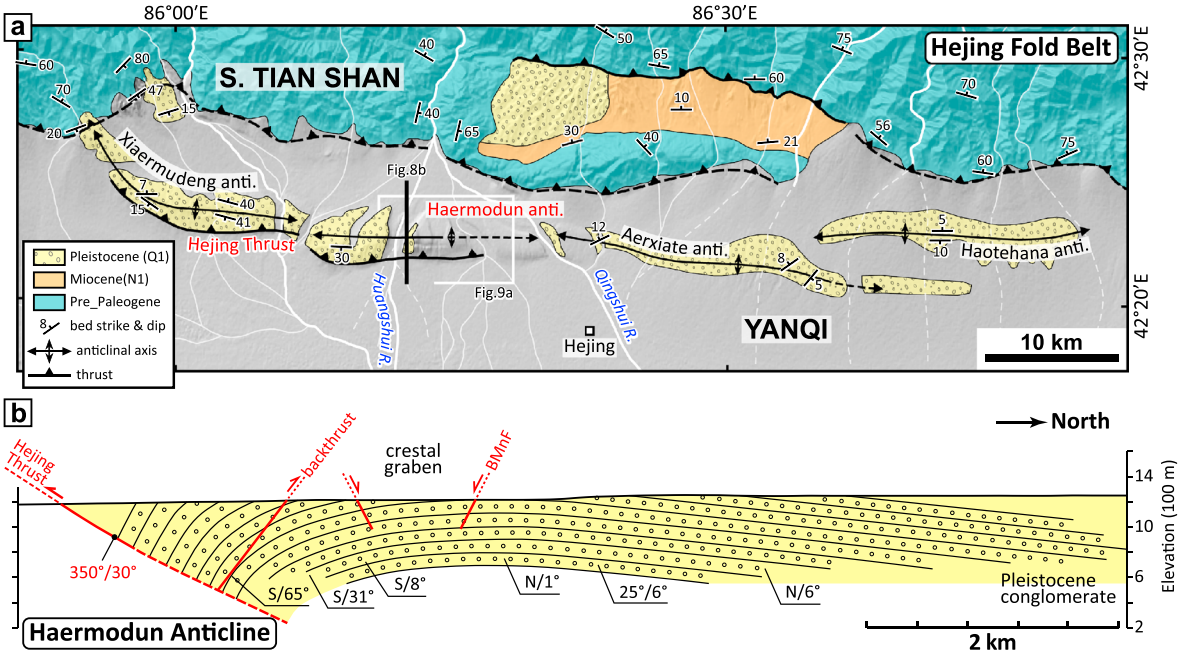

Figure 8. Geologic map of the Hejing fold belt and adjacent structures (see Figure 2 for the map location). (b) Cross section (location in Figure 8a) of the Haermodun anticline defined from field geologic mapping. Modified from Huang et al. (2015). BMnF = bending-moment normal fault.

7. The Haermodun Anticline in the Hejing Fold Belt

The Hejing fold belt deforms the northern margin of the Yanqi Basin, one of the major intermontane basins of the southern Tian Shan (Figures 2 and 8a). The fold belt contains four anticlines that make up one east-trending fold set subparallel with the Tian Shan relief. The topographic expressions of these folds are modest and have a decreasing expression to the east. Our observation is focused on the Haermodun anticline in central west part of the fold belt.

7.1. The Haermodun Anticline

The Haermodun anticline extends eastward for ~18 km (Figure 8a). The fold extensively exposes moderately-lithified Pleistocene conglomerate at its western segment, compared to its eastern segment where only scattered bedrock outcrops are exposed in deep valleys of the south flowing Qingshui and Huangshui Rivers.

Along the Huangshui water gap, structural mapping of the fold depicts a gentle (~6°) northern limb and a relatively steep (~30–60°) southern limb (Figure 8b). Farther south, the ~30°N-dipping Hejing Thrust delineates the leading edge of the southern limb and creates a series of east-trending scarps on the surface. The base of the Pleistocene is not exposed in the fold. We estimated its thickness of $<$600 m at the fold crest referring to the following: (i) the Cenozoic sequence is $<$2,000 m on the fold limb, as constrained from analyses of seismic profiles and borehole data (Li, 2002; B. Yang, 2004); (ii) the Paleogene strata have a relatively stable thickness of 350–500 m across the Yanqi Basin (Li, 2002); and (iii) as illustrated in Figure 8b, the Pleistocene conglomerate at the fold crest is $>$1,000 m thinner than that on the fold's southern limb.

7.2. Folding Deformation of Fluvial Terraces

Draining south from the southern Tian Shan range, the Qingshui and Huangshui Rivers have created four major divisions of fluvial terraces where they cross the Haermodun fold (Figure 9a). The northern portion of these terraces is generally planar and relatively well preserved, compared to their southern portion that has experienced considerable erosion by ephemeral channels. According to cosmogenic ^{10}Be depth profile and luminescence dating results, these terraces, from high to low elevation, were emplaced at ~550, 430, 350, and 60 ka, respectively, indicative of a general correlation between terrace formation and glacial-interglacial transitions (Huang et al., 2014). Beneath the fluvial terraces, dip measurements of limited Pleistocene exposures along the terrace riser approximately define five dip panels (Figure 9c).

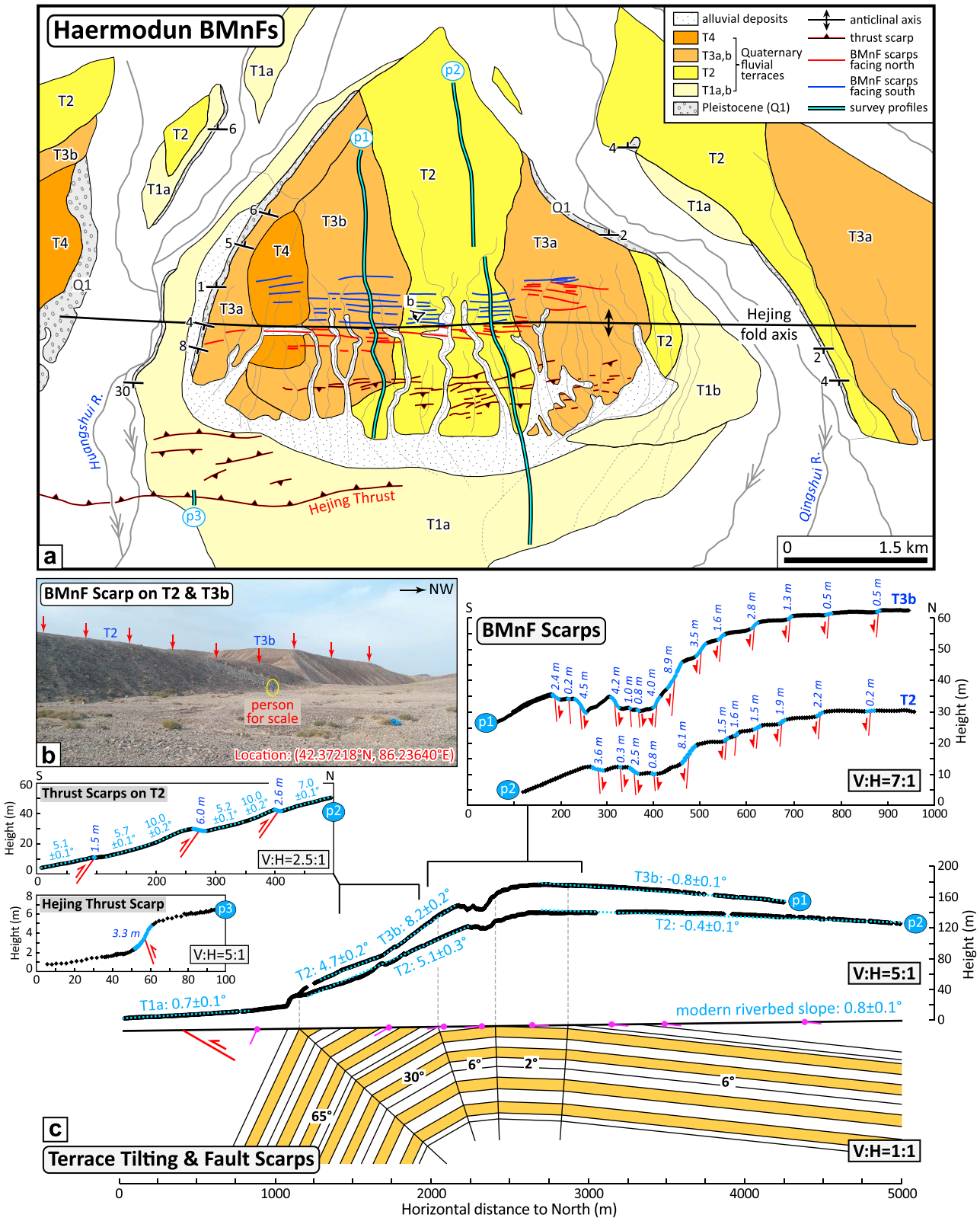

Figure 9. Geologic and geomorphic map of terrace treads and fault scarps in the Haermodun fold. See Figure 8a for the map location. Modified from Huang et al. (2015). (b) Photograph of bending-moment normal fault (BMnF) scarps on the T3b and T2 treads (viewpoint in Figure 9a). The top of BMnF scarps is marked by red arrows. (c) Topographic survey profiles (locations in Figure 9a) of the T3b and T2 treads and underlying fold geometry. The modern riverbed slope of ~0.8° from Huang et al. (2015).

We measured the T3 and T2 treads, the most spatially extensive terraces, to quantify the magnitudes of folding and faulting. In the ~6°N-dipping panel of the northern limb, the T3b and T2 treads slope 0.8 ± 0.1° and 0.4 ± 0.1° to the north, respectively. With respect to the modern, south flowing river slope of 0.8 ± 0.1° determined by Huang et al. (2015), the T3 and T2 treads have been backtilted ~1.6° and 1.2°, respectively. To the south of the anticlinal hinge, these two terraces slope 8.2 ± 0.2° and 4.7–5.1° and have been tilted ~7.4° and 3.9–4.3° in the ~30°S panel, respectively. The differential tilting of each terrace tread and the age-dependent increase of the terrace slope in each dip panel are consistent with the prediction of kinematics of fixed hinge rotation (Figure 3b; e.g., Scharer et al., 2006). Using the uplifted areas enveloped by the T3 (~430 ka) and T2 (~350 ka) treads, Huang et al. (2015) applied the area conversation method to estimate the shortening to be ~120 and 80 m, respectively, corresponding to a uniform shortening rate of ~0.3 mm/a absorbed by folding deformation.

7.3. Faulting Deformation of Fluvial Terraces

In total, three sets of fault scarps have been recognized on the Haermodun fluvial terraces (Figure 9). At the fold crest, a clear graben comprises 4–8 south-facing BMnF scarps and 3–5 north-facing BMnF scarps (Figures 9a and 9c). The south-facing scarps occur in a ~300- to 500-m-wide zone with spacings of 30–180 m, whereas the north-facing scarps occur in a ~90- to 120-m-wide zone with spacings of 30–50 m. In the context of the underlying structure, the south and north facing scarps are roughly located in the ~2°N panel to the north of the anticlinal hinge and the ~6°S panel to the south of the hinge, respectively. The height of these scarps varies from ~0.2 to 8.9 m (Figure 9c). It is noted that several prominent fault scarps with heights of 4–9 m are mainly localized close to the anticlinal hinge, compared to fault scarps with general heights of $<$2.0 m away from the hinge. This height contrast is different from the relatively homogenous heights across the whole fault zone at Slik and the prominent fault scarps bounding the fault zone at Cele, indicating that extension due to BMnFs at this site is more concentrated than that at the above two sites. The summed heights of BMnF scarps are ~36 m on the T3b tread and ~24 m on the T2 tread, accounting for ~10 and ~7 m of extension, respectively. Combining with terrace ages of ~430 and ~350 ka determined by Huang et al. (2014) for the T3b and T2 treads, respectively, an extension rate of ~0.02 mm/a is accommodated by BMnFs.

Approximately 400 m to the south of the crestal graben (Figure 9a), a group of south-side-up, 0.3- to 6.0-m-high fault scarps occur on the T3 and T2 treads. Although these scarps have similar trends and facing directions as the north facing BMnF scarps, we prefer to interpret them as thrust fault scarps, but not BMnF scarps because of the following observations. First, the terrace tread on the upthrown side of each fault is significantly tilted (Figure 9c), features more likely to be characteristic of thrust faulting, rather than BMnFs whose upthrown surface commonly displays little tilted. For example, along the profile *p*2 on the T2 tread (Figure 9c), the terrace slope to the south of the fault can be as high as ~10.0°, much higher than the terrace slope of ~5.1°. Additionally, a clear gap exists between these scarps and the north-facing BMnF scarps, which perhaps indicates a different genetic mechanism because the fault spacing of BMnF scarps typically stays constant or changes gradually along a transect (e.g., Figures 5a and 7a). As discussed in the following paragraph, because these faults thrust to the north, these scarps are probably the secondary back thrusts related to the south-thrusting Hejing Thrust (Figure 8b). The summed height of these scarps is ~10 m on the ~350-ka-old T2 tread, producing a total vertical slip rate of ~0.03 mm/a of these faults.

Farther south, the Hejing Thrust transects the T1a tread (~60 ka) and produces several geomorphic scarps with heights of 0.8–3.3 m (Figures 9a and 9c). These scarps are dominantly south-facing, in spite of one or two north-facing scarps with low heights. Among all fault scarps, the southernmost one is the most well-developed. This scarp can be traced continuously $>$3 km on the T1a tread and even on the Huangshui modern riverbed (Figure 9a). A trench outcrop across the fault reveals a fault dip of ~30° (Huang et al., 2015). If we assume this fault dip is representative of all the thrust faults, the summed height of the fault scarps is ~6 m and the total dip-slip and shortening (horizontal component of the dip-slip) rates of the Hejing Thrust are ~0.2 mm/a. Given that the fault slip rate of ~0.2 mm/a on the Hejing Thrust is comparable to the hanging-wall shortening rate of ~0.3 mm/a, we propose that the Hejing thrust scarps are probably created by near-surface fault splays of the causative fault controlling the growth of the Haermodun anticline. Because the north-facing thrust scarps on the T3 and T2 treads have a similar orientation but opposite-facing direction compared with the Hejing thrust scarps, they are likely the back thrusts of the underlying causative fault. If these back thrusts

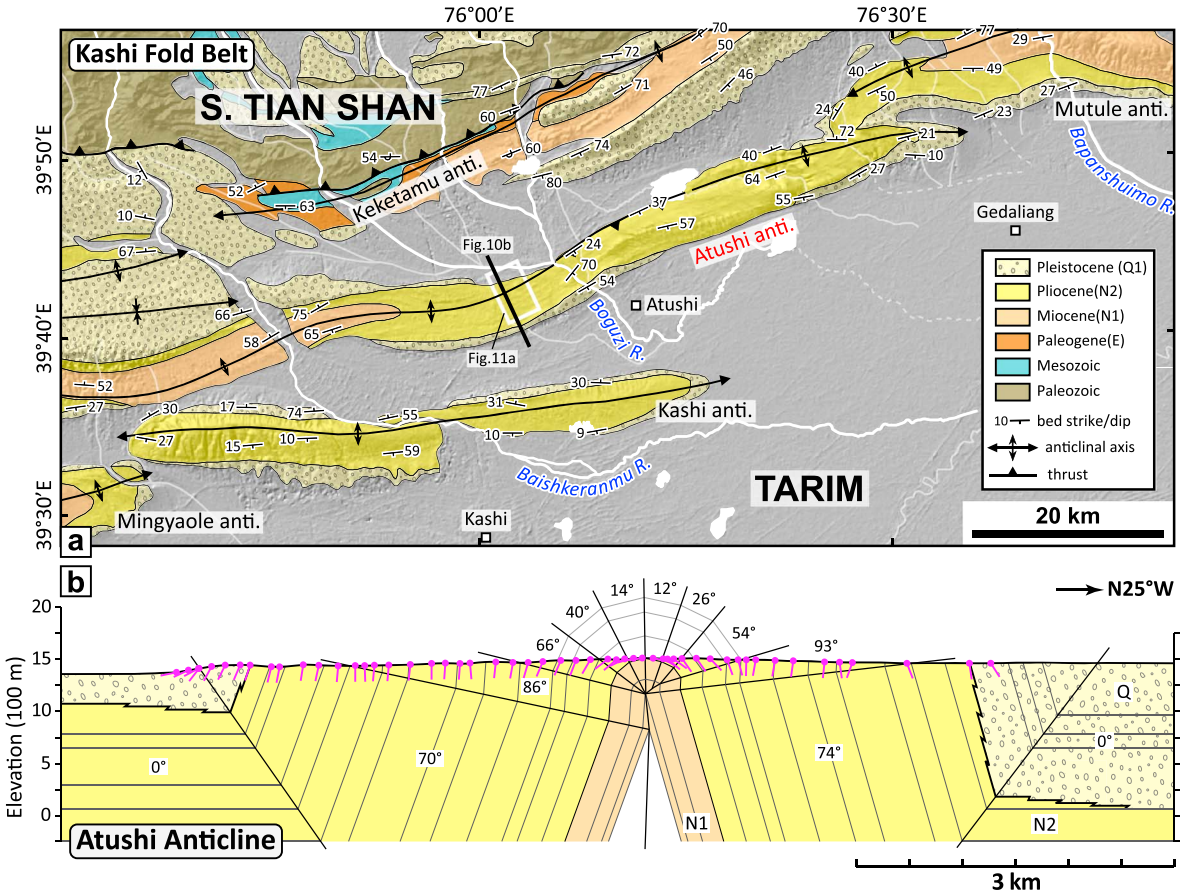

Figure 10. Geologic map of the Kashi fold belt and adjacent structures (see Figure 2 for the map location). (b) Cross section (location in Figure 10a) of the Atushi anticline defined from field geologic mapping.

are assumed to have a fault dip of ~30°, according to the summed thrust scarp heights of ~10 m and the T2 tread age of ~350 ka, the shortening rate (horizontal component of the dip-slip rate) is ~0.05 mm/a.

In summary, analyses of the folded and faulted fluvial terraces on the Hejing fold define a total shortening rate of ~0.55 mm/a, comprising a shortening rate of ~0.2 mm/a on the Hejing Thrust itself, a shortening rate of ~0.05 mm/a on its back thrusts, and a shortening rate of ~0.3 mm/a absorbed by folding deformation on the hanging wall. Therefore, the extension rate of ~0.02 mm/a is only ~4% of the total shortening rate.

8. The Atushi Anticline in the Kashi Fold Belt

Our last observation site is the Kashi fold belt located at the western corner of the Tarim Basin (Figures 2 and 10a). The fold belt includes a set of NE-E trending, *en echelon* anticlines. In contrast to the modest or absent surface expressions at the first three sites, these folds have relatively high topographic relief that extensively exposes lithified beds of the Paleozoic through Pleistocene. The fold belt absorbs an average shortening rate of ~5 mm/a during the Quaternary, and its recent activity is concentrated on the Atushi and Kashi anticlines (Y. Chen et al., 2002; Heermance et al., 2008; Scharer et al., 2006; Thompson-Jobe et al., 2017).

8.1. The Atushi Anticline

With a total length exceeding 100 km, the Atushi anticline extends to the northeast in several gentle arcs and ultimately loses its surface expression beneath alluvial deposits at southern front of the Mutule fold (Figure 10a). Several transverse rivers, including Baishkeranmu and Boguzi Rivers, flow southward to cross the fold and produce broad water gaps.

The Atushi anticline exposes a coarsening upward sedimentary sequence of Miocene through Pleistocene strata (Figure 10a). The Miocene unit in the core is characterized by tan, brownish mudstone, sandy

mudstone and fine sandstone, whereas the Pliocene and Pleistocene units on its two limbs are dominated by gray-yellow and gray-green coarse sandstone alternating with mudstone and gray conglomerates, respectively (Y. Chen et al., 2007; Heermance et al., 2008).

The near-surface structure of the fold is south vergent at its western segment, but north vergent at its eastern segment (Figure 10a). This opposite-vergent geometry is probably because the fold's western segment is controlled by a north-dipping thrust, whereas its eastern segment is associated with a south-dipping back thrust (Heermance et al., 2008; Qian et al., 2008). At the transition zone of these two segments (Figure 10b), however, the fold has a tight core with steep fold limbs (70–93°) that are nearly vertical or overturned in many places, exhibiting an overall box-like geometry with ambiguous vergence. Total shortening appears to decrease eastward along the fold length, which is apparently responsible for the eastward plunging topographic relief and the gradually younging of exposed beds. Through analyses of geologic mapping and magnetostratigraphic data at the Boguzi water gap, Y. Chen et al. (2002) determined a total fold shortening of 4–5 km since the initiation of ~1.4 Ma, yielding an average shortening rate of ~3.3 mm/a.

8.2. Terrace Deformation and Bending-Moment Faulting

Approximately 6 km west of the Boguzi water gap, three levels of fluvial terraces lie on the interbedded sandstone and mudstone of the Pliocene (Figure 11a). All the terraces have been strongly eroded, especially the locally-preserved T2 and T1 treads. The T3 tread, as the most spatially extensive surface, can be traced ~4 km along the fold transect (Heermance et al., 2008). According to cosmogenic ^{10}Be depth profile dating, the T3 tread was abandoned 70–90 ka (Bufe et al., 2017). Despite the presence of terrace levels, the river channel creating them was not been preserved and perhaps was diverted to flow along the fold's northern flank and finally joins the Boguzi River (Figure 10a), in response to continuing uplift of the fold.

Fluvial terraces have been significantly convex-up warped (Figure 11c). A measured profile along the T3 tread defines slopes of $1.8 \pm 0.1°$ and $-2.5 \pm 0.1°$ at either side of the anticlinal hinge. The lack of a nearby modern riverbed that crosses the entire fold makes it impossible to approximate the initial slope of the T3 tread and subsequently evaluate the folding deformation. In this study, we presume the modern fluvial gradient of ~0.6° of the Boguzi River (Scharer et al., 2006) represents the initial T3 slope, considering that the Boguzi River and the river creating the T3 tread cut through the fold close to each other (~8 km) and in similar flow directions (Figure 10a). Consequently, the T3 tread is estimated to be tilted ~1.2° and −3.1° on the southern and northern limbs of the fold, respectively, implying significant rotation of the underlying beds. The convex-shaped T3 tread envelops an uplifted area of ~131,500 m^2 of the fold. Referring to the underlying detachment depth of ~5,000–6,000 m determined from previous interpretations of seismic profiles (e.g., Heermance et al., 2008; Miao et al., 2007; Qian et al., 2008), the mass-conversation method constrains fold shortening to ~24 m (formula (4) and Figure 3b) since abandonment of the T3 tread. Because the T3 tread does not span the entire fold width, this shortening represents a minimum shortening since the terrace abandonment. A combination with the terrace age of 70–90 ka (Bufe et al., 2017) yields a shortening rate of $\geq$0.3 mm/a. This rate appears to be much lower than the average Quaternary shortening rate of ~3.3 mm/a (Y. Chen et al., 2002). One possibility for this discrepancy is because the presently preserved T3 tread spans less than half of the fold (Figure 11c). If the fold shortening is concentrated, for example, near the synclinal hinges where the terrace has not been preserved, the mass-conservation method greatly underestimates the fold shortening. Alternatively, deformation of the Atushi fold may have significantly decelerated since at least 70–90 ka. The remaining shortening was perhaps shifted to the Kashi anticline along the leading edge of the Kashi fold belt or even to somewhere within the Tian Shan.

Near the fold crest, more than 20 BMnF scarps are present in a zone as wide as ~900 m, with fault spacings ranging from 10 to 120 m (Figure 11). Among them, four north-facing scarps with total heights of ~5.5 m and two south-facing scarps with total heights of ~10 m are located immediately to the south and north of the hinge, respectively, to form a prominent graben (Figure 11c). With heights that vary between 0.1 and 1.6 m, fault scarps farther away from the graben, however, are dominantly north-facing to the north of the hinge and south-facing to its south. This distribution pattern of fault-scarp heights is very similar to that on the Haermodun fold, but different from those of the Slik and Cele folds, indicating concentrated extension as well. The summed height of all BMnF scarps is ~22 m along the measured profile, and the corresponding extension is ~6 m, $\leq$25% of the fold shortening of $\geq$24 m.

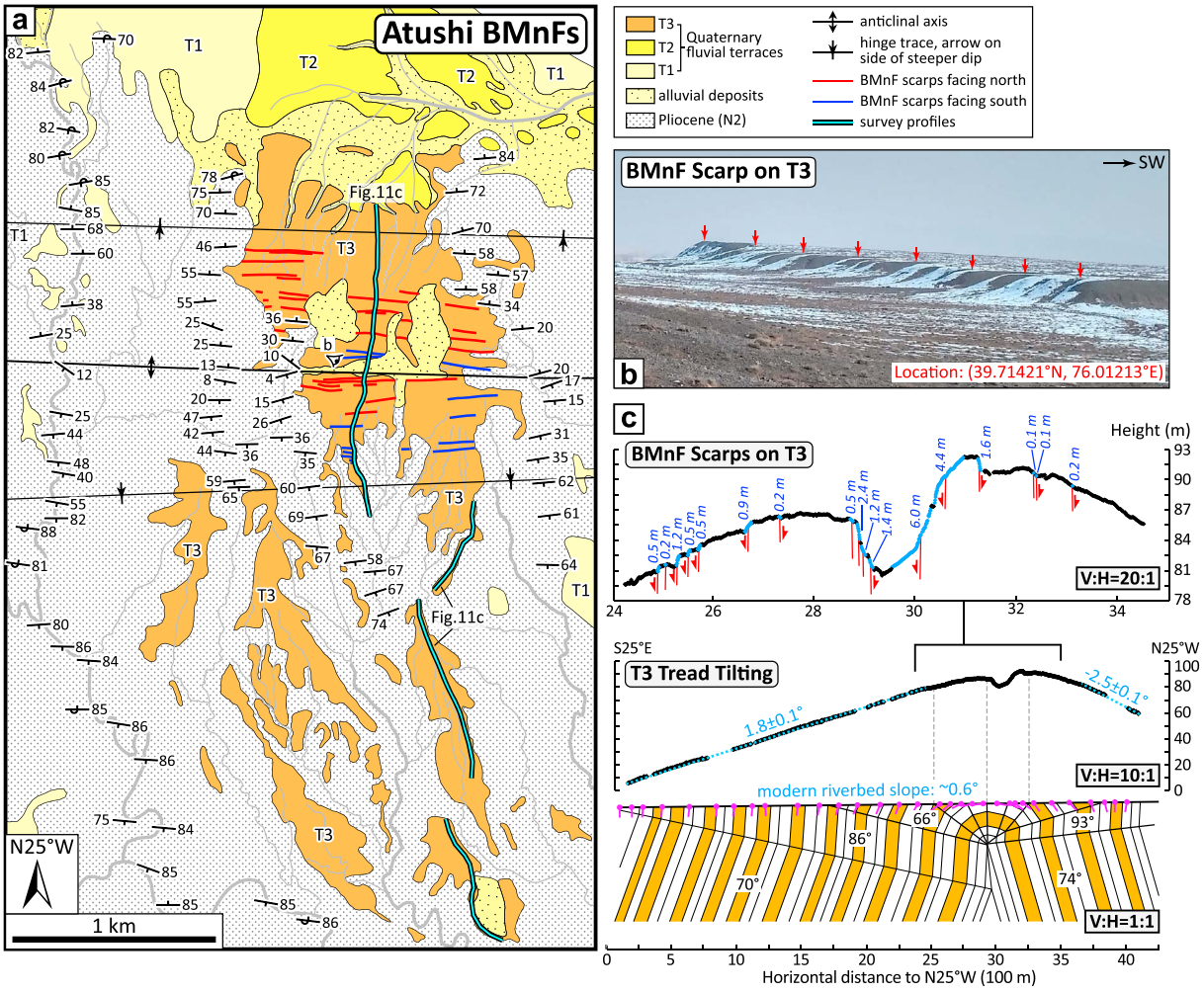

Figure 11. (a) Geologic and geomorphic map of terrace treads and bending-moment normal fault (BMnF) scarps in the Atushi fold. See Figure 10a for the map location. (b) Photograph of a BMnF scarp on the T3 tread (viewpoint in Figure 11a). Red arrows mark the top of the scarp. (c) Topographic survey profiles (locations in Figure 11a) of the T3 tread and underlying fold geometry. The modern riverbed slope of ~0.6° refers to the fluvial gradient of the Boguzi River determined by Scharer et al. (2006).

9. Discussion

The pronounced bending-moment normal fault (BMnF) scarps, along with associated extensively preserved geomorphic surfaces and well-constrained fold geometries at four sites provide an excellent opportunity to investigate the geomorphic expression of BMnF scarps, analyze conditions favorable for their development and summarize their similarities with and differences from those of flexural-slip fault (FSF) scarps.

9.1. Favorable Conditions for the Presence of BMnF Scarps

As suggested by earlier studies, the underlying bed lithology exerts a fundamental control on the basic styles of secondary faults generated by bending-related tangential longitudinal strain (Figure 1): FSFs develop in well-layered beds (e.g., Fischer & Jackson, 1999; Gutiérrez-Alonson & Gross, 1999; Horne & Culshaw, 2001; Tanner, 1989; Tavani et al., 2015), whereas BMFs occur in poorly-layered beds (e.g., Bazalgette et al., 2010; Fischer & Jackson, 1999; Gutiérrez-Alonson & Gross, 1999; Tavani et al., 2015). Our observations in the Pamir-western Kunlun and southern Tian Shan regions demonstrate a good agreement with this generalization. For the BMnF scarps surveyed in this study, with the exception of Atushi where the scarps overlie interbedded Pliocene sandstone and mudstone, the fault scarps at the other three sites overlie massive, poorly-layered Pleistocene or Plio-Pleistocene conglomerate. Conversely, the bed lithology localized FSFs, as examined by our recent study (T. Li et al., 2017), is primarily characterized by well-layered sandstone alternating with mudstone.

The interlimb angle varies significantly across our four folds. The Slik and Cele folds are gentle and broad, and their interlimb angles are as large as ~160° (Figures 4b and 6b). The Haermodun fold, with an interlimb angle of ~110°, is moderately deformed (Figure 8b). Comparatively, the Atushi fold has a fairly tight geometry, whose interlimb angle decreases to $<$40° (Figure 10b). These observations indicate that the BMnF scarps can be generated within both broadly and tightly folded beds, different from FSF scarps which appear to require an underlying bed dip of $>$30° (Figure 13 in T. Li et al., 2017).

BMnF scarps develop when folding kinematics amplify bed curvature to generate convex surface extension (Figure 1; Fossen, 2010; Ramsay, 1967; Tavani et al., 2015). At Haermodun and Atushi, folding deformation is dominated by fixed-hinge rotation, and fluvial terraces and underlying beds are tilted at an angle $>$1.0° (Figures 9c and 11c). The significant decrease of the interlimb angle amplifies the bed curvature to produce BMnF scarps on the land surface (Figure 3b). The Slik and Cele folds are achieved by active-hinge migration. Although the interlimb angle appears to remain invariable, the bed segment moving within the anticlinal hinge zone can increase the curvature itself, thereby producing BMnFs at its convex part (Figure 3a1). Therefore, both progressive fixed-hinge rotation and anticlinal active-hinge migration can produce prominent BMnF scarps. Such BMnF scarps stand in contrast with FSF scarps that are commonly produced during fixed-hinge rotation (T. Li et al., 2017).

In summary, BMnF scarps are expected to occur predominantly above poorly-layered beds but are somewhat independent of the interlimb angle and of the kinematics of fold growth.

9.2. Geomorphic Expressions and Contribution to Fold Shortening

As a result of cutting through the beds, BMnF scarps are typically far more sinuous than FSF scarps. BMnF scarps either do not need to trend strictly parallel with the fold hinge, particularly at locations influenced by shear stress. For example, the Slik fault scarps east of the Pixina water gap and the Cele fault scarps near the Cele water gap tend to align obliquely with the fold hinge (Figures 5a and 7a). In each case, this obliquity can be ascribed to some shear component on the underlying causative thrust.

The BMnF zone can exhibit a half graben, as at Slik or an asymmetric graben, as at Haermodun (Figures 5a and 9a), where all north-facing scarps are clustered and isolated from the grouped south-facing scarps. The BMnF zone can also exhibit grabens alternating with horsts, as at Cele and Atushi, where opposite-facing scarps are mixed (Figures 7a and 11a). Along the lengthen of the fold hinge, the fault zone characterized by a low number of high scarps can transform laterally to the zone characterized by a large number of low scarps, as manifested by the Cele Fault (Figure 7a). Specific reasons for these changing geomorphic expressions at different sites and even along a single fold are currently unknown. One speculative control may be bed lithology: more homogenous beds perhaps facilitate development of grabens, whereas inhomogeneous beds favor grabens alternating with horsts; similarly, competent beds may encourage the formation of a lower number of relatively high scarps, whereas less competent beds promote the formation of numerous, relatively low scarps. The exact controlling factors of these various geomorphic expressions, however, can only be clarified after more field case studies and additional analog modeling.

From Slik to Cele, Haermodun, and Atushi, the fault-zone width and fault spacing tend to clearly decrease, whereas the fault-scarp height near the fold axis tends to significantly increase (Figure 12 and Table 1). At Slik, the width of BMnF zone is 4–7 km at the Pixina water gap, about 30–50% of the fold width of ~13 km. This percentage falls to ~27% (fault-zone width of ~5 km versus the fold width of ~18 km) at Cele but significantly lowers to $<$10% ($<$1 km/~9 km) at Haermodun and Atushi. Accordingly, the fault spacing of 40–1,300 m (average 310 ± 310 m) at Slik and 60–900 m (average 370 ± 240 m) at Cele are much wider than that of 10–90 m (average 40 ± 20 and 50 ± 45 m, respectively) at Haermodun and Atushi (Table 1). The fault-scarp heights are relatively homogenous across the entire fault zone at Slik and are largest at boundaries of the fault zone at Cele, in contrast to those at Haermodun and Atushi where the prominent fault scarps are concentrated near the fold axis, whose heights are much larger than those away from the fold axis. All these features reflect a tendency of the extension from diffusion to concentration.

This tendency is likely accounted by contrasting fold kinematics at the four sites (Figure 12 and Table 1): active-hinge migration at the Slik and Cele versus fixed-hinge rotation at Haermodun and Atushi. As illustrated by numerical models in Salvini and Storti (2004), migration of an active hinge tends to produce a wider and more homogeneous fault zone (Figure 3a1), thus promoting diffusion of the extension, whereas

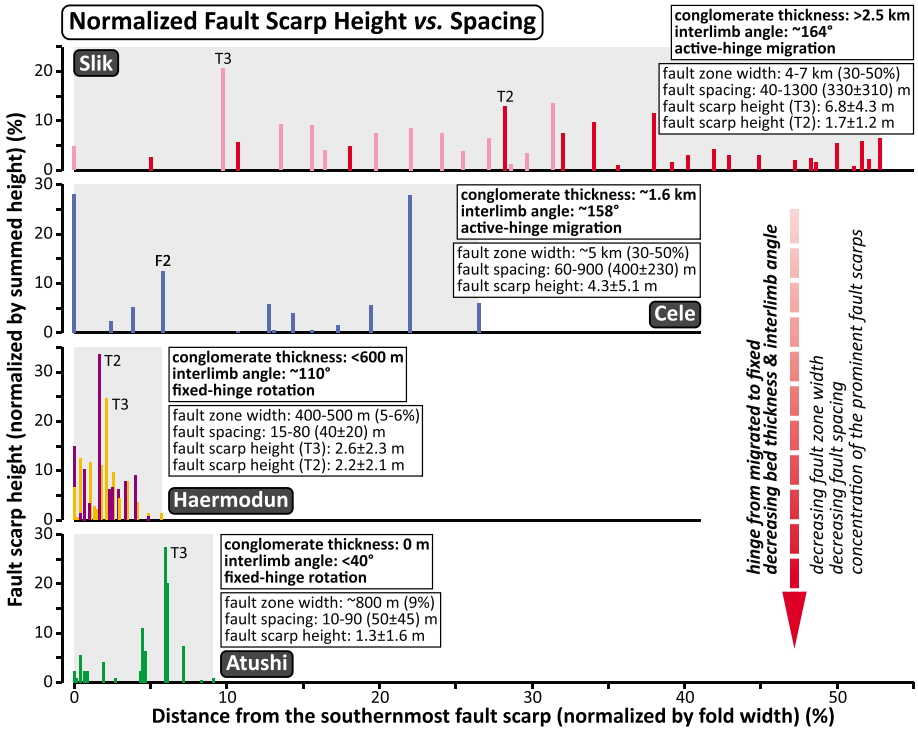

Figure 12. Statistical analyses of BMnF zone width, fault-scarp spacing and height (determined from topographic measured profiles at each site) as a function of the Pleistocene (or Plio-Pleistocene) thickness, interlimb angle, and fold kinematics at four study sites. The gray rectangle area reflects the percentage of fault-zone width relative to the fold width.

rotation around a fixed hinge tends to concentrate the fault zone (extension zone) at the fold crest (Figure 3b). Another critical reason underlying this tendency is the thinning of Pleistocene (or Plio-Pleistocene) conglomerate beneath the land surface and the decreasing interlimb angle: the Pleistocene (or Plio-Pleistocene) thickness decreases gradually from >2,500 m at Slik to ~1,600 m at Cele, <600 m at Haermodun, and 0 m at Atushi. Meanwhile, the interlimb angle decreases from ~160° at Slik and Cele to ~110° at Haermodun and <40° at Atushi. According to Ramsay (1967) and Tavani et al. (2015), the convex-surface extension is a function of the distance to the neutral surface and the bed curvature. Decreasing the bed thickness and interlimb angle can lower the distance to the neutral surface but augment the bed curvature, both of which promote the extension and BMnFs to be restricted in a narrower, more intensively-deformed zone.

Table 1
A Summary of Parameters Associated With Bending-Moment Normal Fault Scarps Reported in This Study

Location	Fold width	Conglomerate thickness	Interlimb angle	Active or fixed hinge	Fault-zone width	Fault spacing	Fault-scarp height	Extension/ shortening
Slik T3	~13 km	2,500-3,000 m	~164°	Active	4-7 km	340±300 m	6.8±4.3 m	~100%
Slik T2						330±320 m	1.7±1.2 m	
Cele F3	~18 km	~1,600 m	~158°	Active	~5 km	1,150±340 m	7.8±4.6 m	~100%
Cele F2						400±230 m	4.3±5.1 m	
Haermodun T3	~9 km	<600 m	~110°	Fixed	400-500 m	40±20 m	2.6±2.3 m	~4%
Haermodun T2						45±20 m	2.2±2.1 m	
Atushi	~9 km	0 m	<40°	Fixed	~800 m	50±45 m	1.3±1.6 m	<25%

10.1029/2018TC004982

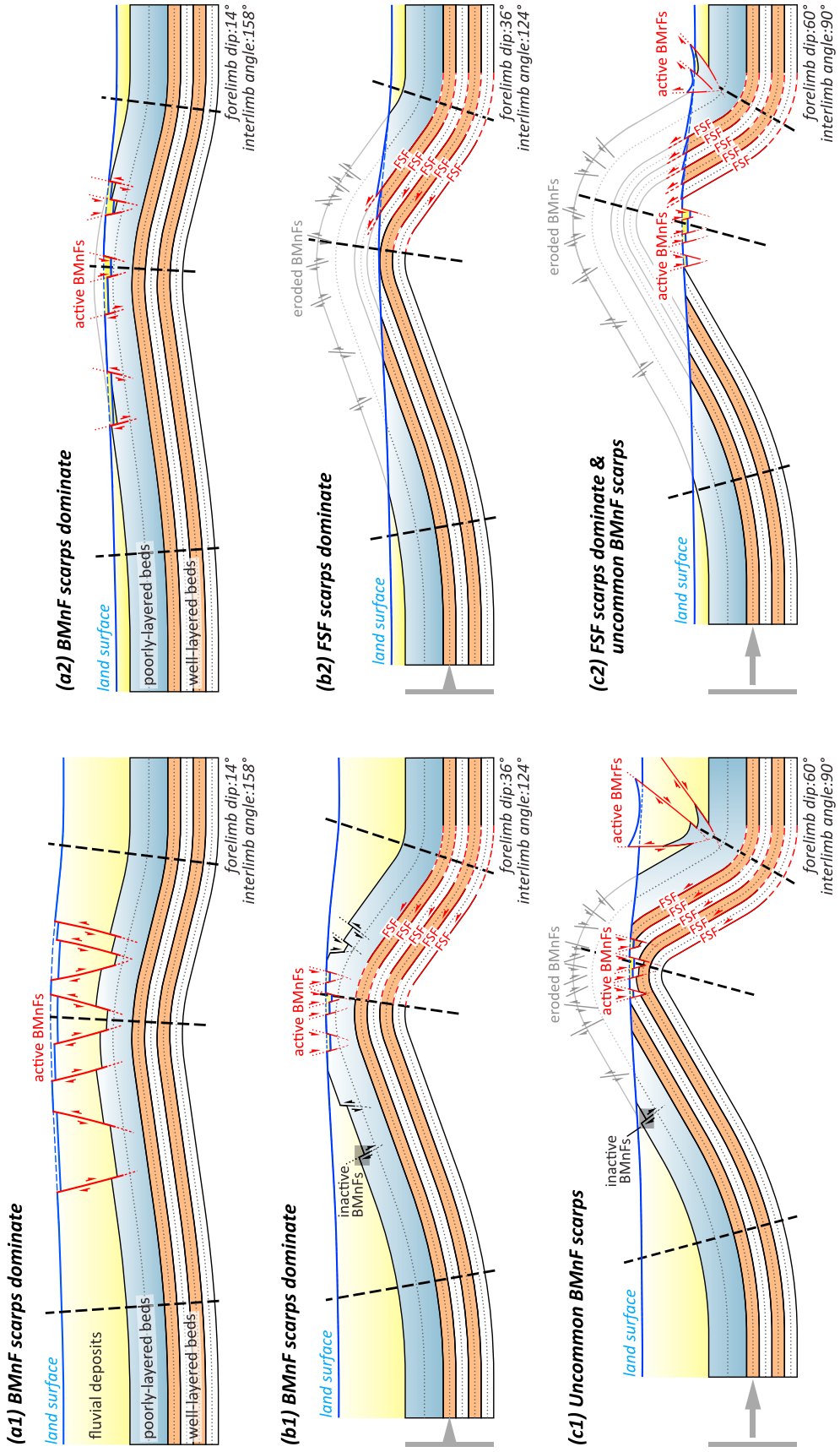

Figure 13. A conceptual model for bending-moment faulting and flexural-slip faulting with progressive fold deformation. (a) At the initiation of folding, bending-moment normal faults (BMnFs) are generated in poorly-layered beds and cut upward through the surface. (b) When the forelimb dip exceeds 30°, flexural slip is activated in well-layered beds. The surface-faulting pattern is dominated by BMnF scarps that overlie the poorly-layered bed (b1) but by flexural-slip fault (FSF) scarps that overlie the well-layered bed (b2). BMnFs distant from the anticlinal hinge cease growth and can be preserved in the folded beds. New faults tend to form near the anticlinal hinge. (c1) With progressive fold tightening, downcutting of the river exposes the well-layered beds. BMnF scarps are uncommonly formed above well-layered beds because of strong fold deformation, and (c2) subsequently with deeper exposures, BMnF scarps can concur with FSF scarps on the fold limb. Formation of the bending-moment reverse faults (BMrFs) are highly speculative given the lack of field case studies. See detailed descriptions in the text.

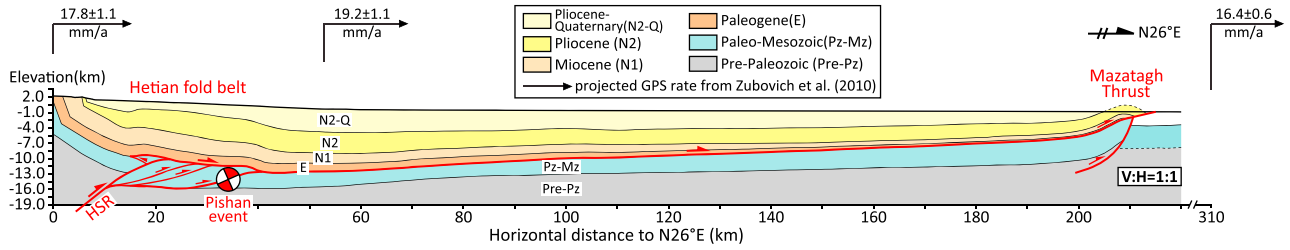

Figure 14. A geologic section across the Hetian fold belt and the Mazatagh Thrust. GPS rates projected to the direction N26°E referring to Zubovich et al. (2010). Modified from T. Li et al. (2016). HSR = Hetian South Ramp.

An additional feature which is probably influenced by bed thickness, interlimb angle, and folding kinematics is the ratio between extension accommodated by BMnFs and fold shortening. At Slik and Cele, the ratio approaches ~100% (Table 1), implying that the extension can even exceed the shortening at the land surface and on the outer surface of the bed. This ratio, however, is only ~4% at Haermodun and $<$ 25% at Atushi. The significant decrease in this ratio indicates a reduced role of BMnFs in the accommodation of fold shortening. Overall, we speculate that, with decreasing bed thickness and interlimb angle and with the transition of fold kinematics from active-hinge migration to fixed-hinge rotation, the BMnFs progressively concentrate within a narrower zone and its efficiency in accommodating folding deformation gradually decreases.

9.3. A Conceptual Model Reconciling Active Bending-Moment Faulting and Flexural Slip

On the basis of above observations, we develop a conceptual model to illustrate the evolution of BMnF scarps during fold growth and specifically to reconcile their presence with the presence of FSF scarps (Figure 13). This model is composed of a thick poorly-layered bed capping on well-layered beds: a scenario consistent with the sedimentary framework in the Pamir-western Kunlun and southern Tian Shan regions, which is typically characterized by Pleistocene (or Plio-Pleistocene) conglomerate overlying interbedded sandstone and mudstone of the Paleo-Neogene (Jia et al., 2004). Our model mainly concerns influences exerted by bed lithology, bed thickness, and fold geometry.

At fold initiation, the fold is gentle and broad (Figure 13a), and bending of the bed can generate sufficient tangential longitudinal strain to produce BMnFs at the convex surface of a poorly-layered bed, as well as associated geomorphic scarps on the land surface. This strain, however, is insufficient to activate flexural slip in well-layered beds. When the forelimb rotates to exceed a dip of ~30° (Figure 13b), flexural slip can be activated along the contacts of well-layered beds, whereas bending-moment faulting can continue in poorly-layered beds. Subsequently following some river incision, if poorly-layered beds can be fully eroded, flexural slip in the underlying well-layered beds can be exposed along with associated geomorphic scarps on the surface (Figure 13b2). Otherwise, the faulting deformation at the surface remains dominated by BMnF scarps (Figure 13b1). With progressive fold uplift and river downcutting, erosion can ultimately breach the poorly-layered bed (Figure 13c). At the fold crest, the BMnF scarps formed previously will have been totally eroded. But, as a result of strong fold deformation, new BMnFs can develop irregularly in well-layered beds and produce associated geomorphic scarps on the surface. On a fold limb where the well-layered beds are extensively exposed, FSF scarps dominate the faulting deformation of the surface (Figure 13c2). These bending-related secondary fault scarps, in conjunction with terrace tilting and warping due to fold deformation, and major fault scarps of the causative thrust, produce complicated geomorphic patterns (e.g., Philip & Meghraoui, 1983).

Our model can explain the spatial distribution of BMnF scarps and FSF scarps in the Pamir-western Kunlun and southern Tian Shan regions (Figure 2). The folds at the western Kunlun piedmont are characterized by low topographic relief and relatively thick Pleistocene (or Plio-Pleistocene) conglomerate (Figures 4a and 6a). This circumstance facilitates the occurrence of BMnF scarps. In the Pamir-Tian Shan convergent zone, contrastingly, strong fold deformation significantly uplifts the bed and extensively exposes well-layered folded beds (T. Li et al., 2017), providing an excellent circumstance for producing FSF scarps.

9.4. Implications to the Geometry and Kinematics of the Western Kunlun Foreland Thrust System

Beyond accommodation in fold deformation, the presence of BMnF scarps can help to delineate the basic fold geometry of the Slik monocline: insights that serve to clarify the geometry and kinematics of the western Kunlun foreland thrust system.

To the north of the western Kunlun range, besides the Hetian fold belt in its piedmont, the Mazatagh Thrust, ~160 km to the north of the Hetian fold belt, emerges from the sand dunes to produce a SEE-trending relief with a total length of >200 km (Figure 2). The relationship between the Hetian fold belt and the Mazatagh Thrust remains contentious (Figure 14). Cheng et al. (2017), Liang et al. (2012), and Lu et al. (2016) interpreted the Hetian fold belt to be a fault-bend fold system wherein a large amount of the fault slip is transferred basinward along a detachment at the base of the Cenozoic sequence and is ultimately consumed by the Mazatagh Thrust. In contrast, Jiang et al. (2013), T. Li et al. (2016), and C. Wang et al. (2014) interpreted that fault slip is likely sent back to the hinterland along a back thrust localized at the base of the Cenozoic, considering that the Mazatagh Thrust is too distant from the Hetian fold belt to be connected by a continuous, low dip angle (1–2°) detachment. In their interpretation, the Mazatagh Thrust is probably formed by the underlying basement-involved thrust system in the Tarim Basin.

The presence of BMnF scarps indicates that the Slik fold is a fault-bend fold, rather than a structural wedge-related fold, and ~4 km of fault slip has been transferred outside the fold (Figures 4b and 14). Because no significant structure exists between the Slik fold and the Mazatagh Thrust, this fault slip would be consumed ultimately by the Mazatagh Thrust. Our study, therefore, provides a credible scenario whereby the Mazatagh Thrust is part of the western Kunlun foreland thrust system. In such a foreland thrust system, the fault slip can be transferred from one structure to the next across a distance of as great as ~160 km along a gently-dipping detachment. This large distance may be assisted (i) by the high syntectonic sediment-accumulation rate on the range piedmont where this rate may have exceeded 1.0 mm/a since the Pliocene (e.g., Fillon et al., 2013; Jiang & Li, 2014; Wu & McClay, 2011; Zheng et al., 2000) and (ii) by the low basal friction of the detachment, which is composed of gypsum and mudstone with thickness of ~300 m (e.g., Buiter, 2012; Cheng et al., 2017; Jia et al., 2004; Liu et al., 1992; Lu et al., 2016). The proposed connection of the Mazatagh Thrust with the Hetian fold belt by the detachment at the base of the Cenozoic sequence supports the speculation of Guilbaud et al. (2017) that mega-earthquakes with magnitudes ≥8 are possible if the fault patch totally ruptures in one single event from the blind ramp of the Hetian fold belt (Hetian South Ramp) to the Mazatagh Thrust (Figure 14). Because the major shortening is consumed by the Mazatagh Thrust, such a geometry could explain the geodetic GPS data showing roughly constant northward velocity across the Hetian fold belt, but a systematic decrease of 2–4 mm/a across the Tarim Basin (Figures 2, 4a, and 14; Zubovich et al., 2010).

The presence of BMnF scarps at Cele also indicates that about ~7 km of fault slip has been transferred basinward. Due to a lack of subsurface data, we are uncertain if this fault slip is ultimately consumed by the Mazatagh Thrust as well.

10. Conclusions

Investigations of clearly expressed bending-moment normal fault (BMnF) scarps at Slik, Cele, Haermodun, and Atushi in the Pamir-western Kunlun and southern Tian Shan regions yield basic but critical insights into the geomorphic expression, controlling conditions, and role in fold accommodation of active bending-moment faulting. Our study indicates the following:

1. BMnF scarps typically have relatively sinuous shapes on the surface compared with flexural-slip fault (FSF) scarps and probably trend obliquely to the fold hinge. A group of BMnFs can exhibit either grabens alternating with horsts or a half or asymmetric graben at different folds, and they can be characterized either by a low number of high scarps or by a large number of low scarps along the same fold.
2. BMnF scarps are primarily observed overlying poorly-layered beds (Pleistocene or Plio-Pleistocene conglomerate), although they are also observed overlying strongly-deformed, well-layered beds (interbedded sandstone and mudstone of the Pliocene). Neither specific fold kinematics nor a particular range of interlimb angles appear to be necessary precursors to these faults, given that observed fold kinematics vary from active-hinge migration to fixed-hinge rotation and the folds' interlimb angles range from ~160° to <40°.

3. For BMnFs, fault-zone width, fault spacing, and the ratio between the extension accommodation by BMnFs versus fold shortening tend to decrease, and the most prominent fault scarps tend to concentrate in a narrow zone, if accompanied by a transition from a migrated to a fixed anticlinal hinge and/or with decreases either in the thickness of poorly-layered conglomerates at or near the surface and/or in the magnitude of the interlimb angle. These trends, individually or in concert, tend to narrow the extension zone at the fold crest and lower the efficiency of fold accommodation.
4. Differences of bed lithology and fold geometry immediately beneath the land surface determine faulting patterns seen at the surface. The low topography of the folds and relative thick Pleistocene (or Plio-Pleistocene) conglomerate in the Western Kunlun piedmont is more likely to produce BMnF scarps, whereas the strongly-deformed folds and extensively-exposed, well-layered beds in the Pamir-Tian Shan convergent zone facilitate FSF scarps.
5. The presence of BMnF scarps suggests that the Slik and Cele folds are fault-bend folds. In this case, a certain amount of fault slip is transferred basinward along a detachment at base of the Cenozoic sequence and probably is absorbed ultimately by the Mazatagh Thrust in the Tarim Basin.

These observations significantly enhance our comprehension of the cohesive relevance between patterns of surface faulting and the underlying bed lithology, thickness, and geometry, even though the causes of apparent linkages are still poorly unknown. For example, why is the BMnF zone characterized by a graben at one site but characterized by grabens alternating with horsts at other sites, or why do a low number of high scarps translate laterally to a large number of low scarps along the same fold? Observations at the western Kunlun piedmont also demonstrate the importance of the analysis of secondary faults in structural interpretations and in determinations of fold kinematics.

Acknowledgments
This study was funded by China NSF (grants 41772196 and 41772221), by Guangdong Province Introduced Innovative R&D Team of Geological Processes and Natural Disasters around the South China Sea (2016ZT06N331), by State Key Lab. of Earthquake Dynamics of China (LED2016A05), and by National S&T Major Project of China (grant 2016ZX05003-001). We thank Y. Yao, B. Zhang, and Q. Liu for their help in the field work. All topographic survey data of terraces in Figures 5, 7, 9, and are available in the supporting information. The original seismic reflection profile across the Cele Normal Fault in Figure b, however, is proprietary and cannot be released to the public according to the policies of PetroChina Company. Thoughtful reviews by A. Hubert-Ferrari and an anonymous reviewer, the Associate Editor, and the Editor L. Jolivet improve this manuscript and are gratefully acknowledged.

References

Ainscoe, E. A., Elliott, J. R., Copley, A., Craig, T. J., Li, T., Parsons, B. E., & Walker, R. T. (2017). Blind thrusting, surface folding, and the development of geological structure in the M_w 6.3 2015 Pishan (China) earthquake. *Journal of Geophysical Research: Solid Earth*, *122*, 9359–9382. https://doi.org/10.1002/2017JB014268

Allen, M. B., Windley, B. F., & Chi, Z. (1999). Late Cenozoic tectonics of the Kepingtage thrust zone: Interactions of the Tien Shan and Tarim Basin, northwest China. *Tectonics*, *18*(4), 639–654. https://doi.org/10.1029/1999TC900019

Audin, L., Herail, G., Riquelme, R., Darrozes, J., Martinod, J., & Font, E. (2003). Geomorphological markers of faulting and neotectonic activity along the western Andean margin, northern Chile. *Journal of Quaternary Science*, *18*(8), 681–694. https://doi.org/10.1002/jqs.787

Avouac, J.-P., & Peltzer, G. (1993). Active tectonics in southern Xinjiang, China: Analysis of terrace riser and normal fault scarp degradation along the Hotan-Qira fault system. *Journal of Geophysical Research*, *98*(B12), 21,773–21,807. https://doi.org/10.1029/93JB02172

Bazalgette, L., Petit, J., Amrhar, M., & Ouanaïmi, H. (2010). Aspects and origins of fractured dip-domain boundaries in folded carbonate rocks. *Journal of Structural Geology*, *32*(4), 523–536. https://doi.org/10.1016/j.jsg.2010.03.002

Bufe, A., Burbank, D. W., Liu, L., Bookhagen, B., Qin, J., Chen, J., et al. (2017). Variations of lateral bedrock erosion rates control planation of uplifting folds in the foreland of the Tian Shan, NW China. *Journal of Geophysical Research: Earth Surface*, *122*, 2431–2467. https://doi.org/10.1002/2016JF004099

Buiter, S. (2012). A review of brittle compressional wedge models. *Tectonophysics*, *530-531*, 1–517. https://doi.org/10.1016/j.tecto.2011.12.018

Cao, K., Wang, G., Bernet, M., Van Der Beek, P., & Zhang, K. (2015). Exhumation history of the West Kunlun Mountains, northwestern Tibet: Evidence for a long-lived, rejuvenated orogen. *Earth and Planetary Science Letters*, *432*, 391–403. https://doi.org/10.1016/j.epsl.2015.10.033

Chen, H., Luo, J., Guo, Q., Liao, L., Xiao, Z., Cheng, X., et al. (2009). Deformation history and tectonic evolution of southern Tarim basin in Mesozoic and Cenozoic [in Chinese]. *Geotectonica et Metallogenia*, *33*(1), 38–45.

Chen, J., Burbank, D. W., Scharer, K. M., Sobel, E., Yin, J., Rubin, C., & Zhao, R. (2002). Magnetochronology of the Upper Cenozoic strata in the Southern Chinese Tian Shan: Rates of Pleistocene folding and thrusting. *Earth and Planetary Science Letters*, *195*(1-2), 113–130. https://doi.org/10.1016/S0012-821X(01)00579-9

Chen, J., Heermance, R., Burbank, D. W., Scharer, K. M., Miao, J., & Wang, C. S. (2007). Quantification of growth and lateral propagation of the Kashi anticline, southwest Chinese Tian Shan. *Journal of Geophysical Research*, *112*, B03S16. https://doi.org/10.1029/2006JB004345

Cheng, X., Chen, H., Lin, X., Wu, L., & Gong, J. (2017). Geometry and kinematic evolution of the Hotan-Tiklik segment of the western Kunlun thrust belt: Constrained by structural analyses and apatite fission track thermochronology. *The Journal of Geology*, *125*(1), 65–82. https://doi.org/10.1086/689187

Cheng, X., Liao, L., Chen, H., Chen, L., Yang, S., Wang, B., et al. (2008). Research of Cenozoic structural deformation in southeastern Tarim basin, northwest China [in Chinese]. *Acta Petrologica Sinica*, *24*(4), 645–654.

Davis, G. H., Reynolds, S. J., & Kluth, C. F. (2012). *Structural geology of rocks and regions* (3rd ed., p. 839). Hoboken, NJ: John Wiley.

Dumitru, T. A., Zhou, D., Chang, E. Z., Graham, S. A., Hendrix, M. S., Sobel, E. R., & Carroll, A. R. (2001). Uplift, exhumation, and deformation in the Chinese Tian Shan. In M. S. Hendrix, & G. A. Davis (Eds.), *Paleozoic and mesozoic tectonic evolution of central and eastern Asia: From continental assembly to intracontinental deformation*, *Geological Society of America memoir* (Vol. 194, pp. 71–99). https://doi.org/10.1130/0-8137-1194-0.71

Epard, J. L., & Groshong, R. H. (1993). Excess area and depth to detachment. *The American Association of Petroleum Geologists Bulletin*, *77*(4), 1291–1302.

Fillon, C., Huismans, R. S., & Van Der Beek, P. (2013). Syntectonic sedimentation effects on the growth of fold-and-thrust belts. *Geology*, *41*(1), 83–86. https://doi.org/10.1130/G33531.1

Fischer, M. P., & Jackson, P. B. (1999). Stratigraphic controls on deformation patterns in fault-related folds: A detachment fold example from the Sierra Madre Oriental, northeast Mexico. *Journal of Structural Geology*, *21*(6), 613–633. https://doi.org/10.1016/S0191-8141(99)00044-9

Fossen, H. (2010). *Structural geology*. Cambridge: Cambrige University Press. https://doi.org/10.1017/CBO9780511777806
Gan, W., Zhang, P., Shen, Z., Niu, Z., Wang, M., Wan, Y., et al. (2007). Present-day crustal motion within the Tibetan plateau inferred from GPS measurements. *Journal of Geophysical Research*, *112*, B08416. https://doi.org/10.1029/2005JB004120
Goode, J. K., Burbank, D. W., & Ormukov, C. (2014). Pliocene-Pleistocene initiation, style, and sequencing of deformation in the central Tien Shan. *Tectonics*, *33*, 464–484. https://doi.org/10.1002/2013TC003394
Grützner, C., Walker, R. T., Abdrakhmatov, K. E., Mukambaev, A., Elliott, A. J., & Elliott, J. R. (2017). Active tectonics around Almaty and along the Zailisky Alatau rangefront. *Tectonics*, *36*, 2192–2226. https://doi.org/10.1002/2017TC004657
Guilbaud, C., Simoes, M., Barrier, L., Laborde, A., Van der Woerd, J., Li, H., et al. (2017). Kinematics of active deformation across the western Kunlun mountain range (Xinjiang, China), and potential seismic hazards within the southern Tarim Basin. *Journal of Geophysical Research: Solid Earth*, *122*, 10,398–10,426. https://doi.org/10.1002/2017JB014069
Gutiérrez, F., Carbonel, D., Mirkeham, R. M., Guerrero, J., Lucha, P., & Matthews, V. (2014). Can flexural-slip faults related to evaporite dissolution generate hazardous earthquakes? The case of the Grand Hogback monocline of west-central Colorado. *Geological Society of America Bulletin*, *126*(11–12), 1481–1494. https://doi.org/10.1130/B31054.1
Gutiérrez-Alonson, G., & Gross, M. R. (1999). Structures and mechanisms associated with development of a fold in the Cantabrian Zone thrust belt, NW Spain. *Journal of Structural Geology*, *21*(6), 653–670. https://doi.org/10.1016/S0191-8141(99)00055-3
He, P., Wang, Q., Ding, K., Li, J., & Zou, R. (2016). Coseismic and postseismic slip ruptures for 2015 *M*w 6.4 Pishan earthquake constrained by static GPS solutions. *Geodesy and Geodynamics*, *7*(5), 323–328. https://doi.org/10.1016/j.geog.2016.07.004
He, P., Wang, Q., Ding, K., Wang, M., Qiao, X., Li, J., et al. (2016). Source model of the 2015 M_w 6.4 Pishan earthquake constrained by interferometric synthetic aperture radar and GPS: Insight into blind rupture in the western Kunlun Shan. *Geophysical Research Letters*, *43*, 1511–1519. https://doi.org/10.1002/2015GL067140
Heermance, R. V., Chen, J., Burbank, D. W., & Miao, J. J. (2008). Temporal constraints and pulsed Late Cenozoic deformation during the structural disruption of the active Kashi foreland, northwest China. *Tectonics*, *27*, TC6012. https://doi.org/10.1029/2007TC002226
Horne, R., & Culshaw, N. (2001). Flexural-slip folding in the Meguma Group, Nova Scotia, Canada. *Journal of Structural Geology*, *23*(10), 1631–1652. https://doi.org/10.1016/S0191-8141(01)00017-7
Huang, W., Yang, X., Li, A., Pierce, I., Thompson, J. A., Angster, S. J., & Zhang, L. (2015). Late Pleistocene shortening rate on the northern margin of the Yanqi Basin, southeastern Tian Shan, NW China. *Journal of Asian Earth Sciences*, *112*, 11–24. https://doi.org/10.1016/j.jseaes.2015.08.024
Huang, W., Yang, X., Li, A., Thompson, J. A., & Zhang, L. (2014). Climatically controlled formation of river terraces in a tectonically active region along the southern piedmont of the Tian Shan, NW China. *Geomorphology*, *220*, 15–29. https://doi.org/10.1016/j.geomorph.2014.05.024
Hubert-Ferrari, A., Suppe, J., Gonzalez-Mieres, R., & Wang, X. (2007). Mechanisms of active folding of the landscape (southern Tian Shan, China). *Journal of Geophysical Research*, *112*, B03S09. https://doi.org/10.1029/2006JB004362
Hubert-Ferrari, A., Suppe, J., Van Der Woerd, J., Wang, X., & Lu, H. (2005). Irregular earthquake cycle along the southern Tian Shan front, Aksu area, China. *Journal of Geophysical Research*, *110*, B06402. https://doi.org/10.1029/2003JB002603
Ismat, Z. (2008). Folding kinematics expressed in fracture patterns: An example from the Anti-Atlas fold belt, Morocco. *Journal of Structural Geology*, *30*(11), 1396–1404. https://doi.org/10.1016/j.jsg.2008.07.010
Jia, C., Zhang, S., & Wu, S. (2004). *Stratigraphy of the Tarim Basin and adjacent areas* [in Chinese] (1063 pp.). Beijing: Science Press.
Jiang, X., & Li, Z. (2014). Seismic reflection data support episodic and simultaneous growth of the Tibetan plateau since 25 Myr. *Nature Communications*, *5*(1), 5453. https://doi.org/10.1038/ncomms6453
Jiang, X., Li, Z., & Li, H. (2013). Uplift of the west Kunlun range, northern Tibetan plateau, dominated by brittle thickening of the upper crust. *Geology*, *41*(4), 439–442. https://doi.org/10.1130/G33890.1
Kelsey, H. M., Sherrod, B. L., Nelson, A. R., & Brocher, T. M. (2008). Earthquakes generated from bedding plane-parallel reverse faults above an active wedge thrust, Seattle fault zone. *Geological Society of America Bulletin*, *120*(11–12), 1581–1597. https://doi.org/10.1130/B26282.1
Li, T., Chen, J., Fang, L., Chen, Z., Thompson, J. A., & Jia, C. (2016). The 2015 M_w 6.4 Pishan earthquake: Seismic hazards of active blind wedge thrust system at the western Kunlun range front, northwest Tibetan Plateau. *Seismological Research Letters*, *87*(3), 601–608. https://doi.org/10.1785/0220150205
Li, T., Chen, J., Thompson, J. A., Burbank, D. W., & Xiao, W. P. (2012). Equivalency of geologic and geodetic rates in contractional orogens: New insights from the Pamir Frontal Thrust. *Geophysical Research Letters*, *39*, L15305. https://doi.org/10.1029/2012GL051782
Li, T., Chen, J., Thompson, J. A., Burbank, D. W., & Yang, X. (2013). Quantification of three-dimensional folding using fluvial terraces: A case study from the Mushi anticline, northern margin of the Chinese Pamir. *Journal of Geophysical Research*, *112*, 4628–4647. https://doi.org/10.1002/jgrb.50316
Li, T., Chen, J., Thompson, J. A., Burbank, D. W., & Yang, H. (2015a). Hinge-migrated fold-scarp model based on an analysis of bed geometry: A study from the Mingyaole anticline, southern foreland of Chinese Tian Shan. *Journal of Geophysical Research: Solid Earth*, *120*, 6592–6613. https://doi.org/10.1002/2015JB012102
Li, T., Chen, J., Thompson, J. A., Burbank, D. W., & Yang, X. (2015b). Active flexural-slip faulting: A study from the Pamir-tian Shan convergent zone, NW China. *Journal of Geophysical Research: Solid Earth*, *120*, 4359–4378. https://doi.org/10.1002/2014JB011632
Li, T., Chen, J., Thompson Jobe, J. A., & Burbank, D. W. (2017). Active flexural-slip faulting: Controls exerted by stratigraphy, geometry, and fold kinematics. *Journal of Geophysical Research: Solid Earth*, *122*, 8538–8565. https://doi.org/10.1002/2017JB013966
Li, Y. (2002). Research on structural evolution and petroleum system in Yanqi basin, Xinjiang [in Chinese]. PhD thesis, China University of Geosciences (Beijing).
Liang, H., Du, Z., Wang, Y., & Wang, Y. (2012). Cenozoic fold and thrust belt in eastern section of the piedmont of west Kunlun and its taper wedge mechanics [in Chinese]. *Chinese Journal of Geology*, *47*, 808–823.
Liu, H., McClay, K. R., & Powell, D. (1992). Physical models of thrust wedges. In K. R. McClay (Ed.), *Thrust tectonics* (pp. 71–81). London: Chapman & Hall.
Livio, F., Kettermann, M., Reicherter, K., & Urai, J. (2018). Growth of bending-moment faults due to progressive folding: Insights from sandbox models and paleoseismological implications. *Geomorphology*. https://doi.org/10.1016/j.geomorph.2018.02.012
Lu, R., Xu, X., He, D., Liu, B., Tan, X., & Wang, X. (2016). Co-seismic and blind fault of the 2015 Pishan M_w 6.5 earthquake: Implications for the sedimentary- tectonic framework of the western Kunlun Mountains, northern Tibetan Plateau. *Tectonics*, *35*, 956–964. https://doi.org/10.1002/2015TC004053
McCalpin, J. M. (2009). *Paleoseismology*, *International geophysics series* (2nd ed., p. 798). Amsterdam: Elsevier Publishing.
Miao, J., Jia, C., Hou, X., Wang, Z., Zou, C., Tang, L., & Song, Y. (2007). Structural analysis on Cenzoic fold-and-thrust belts in Kashi area, western Tarim basin. *Chinese Journal of Geology*, *42*, 740–752.
Philip, H., & Meghraoui, M. (1983). Structural analysis and interpretation of the surface deformations of the El Asnam earthquake of October 10, 1980. *Tectonics*, *2*(1), 17–49. https://doi.org/10.1029/TC002i001p00017

Poblet, J., & McClay, K. (1996). Geometry and kinematics of single-layer detachment folds. *American Association of Petroleum Geologists Bulletin*, *80*, 1085–1109.
Qian, J., Xiao, A., Cheng, X., Wang, L., Zhang, W., Meng, L., & Yao, Q. (2008). Structural deformation of fold-thrust belt in the north margin of Kashi, southern Tian Shan. *Journal of China University of Mining and Technology*, *37*(4), 538–544.
Ramsay, J. G. (1967). *Folding and fracturing of rocks*. New York: McGrawHill.
Saint-Carlier, D., Charreau, J., Lavé, J., Blard, P., Dominguez, S., Avouac, J., et al. (2016). Major temporal variations in shortening rate absorbed along a large active fold of the southeastern Tianshan piedmont (China). *Earth and Planetary Science Letters*, *434*, 333–348. https://doi.org/10.1016/j.epsl.2015.11.041
Salvini, F., & Storti, F. (2004). Active-hinge-folding-related deformation and its role in hydrocarbon exploration and development-Insights from HCA modeling. In K. R. McClay, J. Shaw, & J. Suppe (Eds.), *Thrust fault-related folding (AAPG Mem)* (pp. 463–482).
Scharer, K. M., Burbank, D. W., Chen, J., & Weldon, R. J. II (2006). Kinematic models of fluvial terraces over active detachment fold: Constraints on the growth mechanism of the Kashi-Atushi fold system, Chinese Tian Shan. *Geological Society of America Bulletin*, *118*(7–8), 1006–1021. https://doi.org/10.1130/B25835.1
Scharer, K. M., Burbank, D. W., Chen, J., Weldon, R. J., Rubin, C., Zhao, R., & Shen, J. (2004). Detachment folding in the southwestern Tian Shan-Tarim foreland, China: Shortening estimates and rates. *Journal of Structural Geology*, *26*(11), 2119–2137. https://doi.org/10.1016/j.jsg.2004.02.016
Shaw, J. H., Connors, C., & Suppe, J. (2005). *Seismic interpretation of contractional fault-related folds*, *AAPG studies in geology* (Vol. 53). Tulsa, OK: American Association of Petroleum Geologists.
Sobel, E. R., Chen, J., & Heermance, R. V. (2006). Late Oligocene-Early Miocene initiation of shortening in the southwestern Chinese Tian Shan: Implications for Neogene shortening rate variations. *Earth and Planetary Science Letters*, *247*(1–2), 70–81. https://doi.org/10.1016/j.epsl.2006.03.048
Sobel, E. R., Chen, J., Schoenbohm, L. M., Thiede, R., Stockli, D. F., Sudo, M., & Strecker, M. (2013). Oceanic-style subduction controls late Cenzoic deformation of the Northern Pamir orogen. *Earth and Planetary Science Letters*, *363*, 204–218. https://doi.org/10.1016/j.epsl.2012.12.009
Suppe, J. (1983). Geometry and kinematics of fault-bend folding. *American Journal of Science*, *283*(7), 684–721. https://doi.org/10.2475/ajs.283.7.684
Suppe, J., Sabat, F., Munoz, J. A., Poblet, J., Roca, E., & Verges, J. (1997). Bed-by-bed fold growth by kink-band migration: Sant Llorenc de Morunys, eastern Pyrenees. *Journal of Structural Geology*, *19*(3–4), 443–461. https://doi.org/10.1016/S0191-8141(96)00103-4
Tanner, P. (1989). The flexural-slip mechanism. *Journal of Structural Geology*, *11*(6), 635–655. https://doi.org/10.1016/0191-8141(89)90001-1
Tavani, S., Storti, F., Lacombe, O., Corradetti, A., Muñoz, J. A., & Mazzoli, S. (2015). A review of deformation pattern templates in foreland basin systems and fold-and-thrust belts: Implications for the state of stress in the frontal regions of thrust wedges. *Earth-Science Reviews*, *141*, 82–104. https://doi.org/10.1016/j.earscirev.2014.11.013
Thompson, J. A., Burbank, D. W., Li, T., Chen, J., & Bookhagen, B. (2015). Late Miocene northward propagation of the northeast Pamir thrust system, Northwest China. *Tectonics*, *34*, 510–534. https://doi.org/10.1002/2014TC003690
Thompson, S. C., Weldon, R. J., Rubin, C. M., Abdrakhmatov, K., Molnar, P., & Berger, G. W. (2002). Late Quaternary slip rates across the central Tien Shan, Kyrgyzstan, central Asia. *Journal of Geophysical Research*, *107* (B9), 2203. https://doi.org/10.1029/2001JB000596
Thompson-Jobe, J. A., Li, T., Chen, J., Burbank, D., & Bufe, A. (2017). Quaternary tectonic evolution of the Pamir-Tian Shan collision zone, northwest China. *Tectonics*, *36*, 2748–2776. https://doi.org/10.1002/2017TC004541
Wang, C., Dai, J., Zhao, X., Li, Y., Graham, S. A., He, D., et al. (2014). Outward-growth of the Tibetan Plateau during the Cenozoic: A review. *Tectonophysics*, *621*, 1–43. https://doi.org/10.1016/j.tecto.2014.01.036
Wang, X., Suppe, J., Guan, S. W., Hubert-ferrari, A., & Jia, C. (2011). Cenozoic structure and tectonic evolution of the Kuqa foldbelt, southern Tianshan, China. In K. R. McClay, J. Shaw, & J. Suppe (Eds.), *Thrust fault-related folding*, *AAPG Mem* (pp. 215–243).
Wei, H. H., Meng, Q., Ding, L., & Li, Z. (2013). Tertiary evolution of the western Tarim basin, northwest China: A tectono-sedimentary response to northward indentation of the Pamir salient. *Tectonics*, *32*, 558–575. https://doi.org/10.1002/tect.20046
Wu, J. E., & McClay, K. R. (2011). In K. R. McClay, J. Shaw, & J. Suppe (Eds.), *Thrust fault-related folding*, *AAPG Mem* (pp. 301–333).
Yang, B. (2004). Tectonic evolution and petroleum accumulation in Mesozoic and Cenzoic Yanqi basin [in Chinese]. PhD thesis, Northwest University, Xi'an.
Yang, S., Chen, L., Xiao, Z., Luo, J., Chen, H., Wang, B., et al. (2009). The Cenozoic fault system of southeastern Tarim Basin [in Chinese]. *Geotectonica et Metalogenia*, *33*(1), 33–37.
Yang, S. M., Li, J., & Wang, Q. (2008). The deformation pattern and fault rate in the Tianshan Mountains inferred from GPS observations. *Science in China Series D*, *51*(8), 1064–1080. https://doi.org/10.1007/s11430-008-0090-8
Yeats, R. S., Sieh, K. S., & Allen, C. R. (1997). *The Geology of earthquakes*, (pp. 344–347). New York: Oxford University Press.
Yin, A., Nie, S., Craig, P., Harrison, T. M., Ryerson, F. J., Qian, X., & Yang, G. (1998). Late Cenozoic tectonic evolution of the southern Chinese Tian Shan. *Tectonics*, *17*(1), 1–27. https://doi.org/10.1029/97TC03140
Zheng, H., Powell, C., An, Z., Zhou, J., & Dong, G. (2000). Pliocene uplift of the northern Tibetan plateau. *Geology*, *28*(8), 715–718. https://doi.org/10.1130/0091-7613(2000)28<715:PUOTNT>2.0.CO;2
Zubovich, A. V., Wang, X.-Q., Scherba, Y. G., Schelochkov, G. G., Reilinger, R., Reigber, C., et al. (2010). GPS velocity field for the Tien Shan and surrounding regions. *Tectonics*, *29*, TC6014. https://doi.org/10.1029/2010TC002772